G4SPLAT: GEOMETRY-GUIDED GAUSSIAN SPLATTING WITH GENERATIVE PRIOR

Anonymous authors
Paper under double-blind review

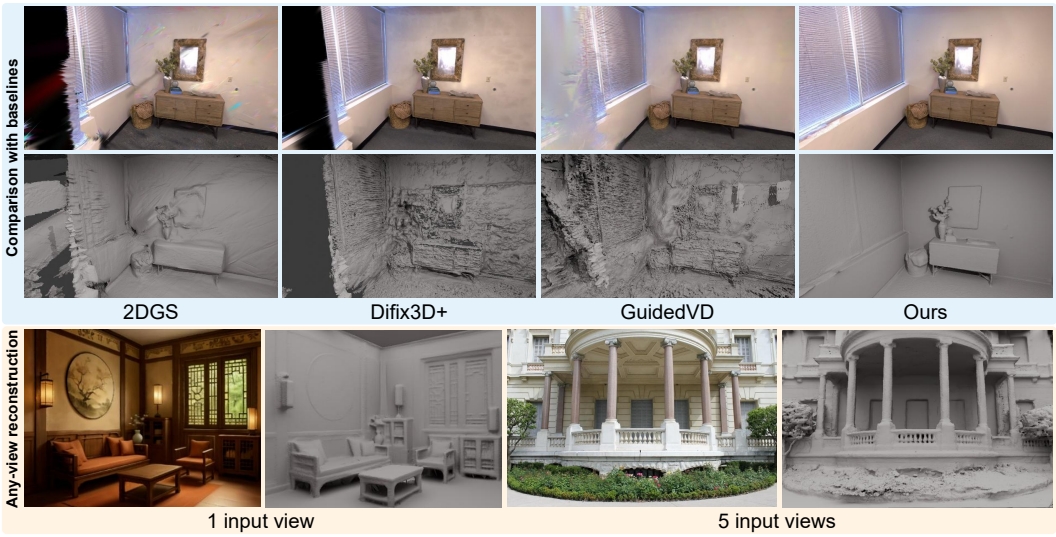

Figure 1: We propose **G4SPLAT**, which integrates accurate geometry guidance with generative prior to enhance 3D scene reconstruction. Our method significantly improves geometry and appearance reconstruction quality in both observed and unobserved regions (black areas in baselines), and generalizes well across diverse scenarios, including *single-view scenes* and *unposed videos*.

ABSTRACT

Despite recent advances in leveraging generative prior from pre-trained diffusion models for 3D scene reconstruction, existing methods still face two critical limitations. First, due to the lack of reliable geometric supervision, they struggle to produce high-quality reconstructions even in observed regions, let alone in unobserved areas. Second, they lack effective mechanisms to mitigate multi-view inconsistencies in the generated images, leading to severe shape–appearance ambiguities and degraded scene geometry. In this paper, we identify accurate geometry as the fundamental prerequisite for effectively exploiting generative models to enhance 3D scene reconstruction. We first propose to leverage the prevalence of planar structures to derive accurate metric-scale depth maps, providing reliable supervision in both observed and unobserved regions. Furthermore, we incorporate this geometry guidance throughout the generative pipeline to improve visibility mask estimation, guide novel view selection, and enhance multi-view consistency when inpainting with video diffusion models, resulting in accurate and consistent scene completion. Extensive experiments on Replica, ScanNet++, and DeepBlending show that our method consistently outperforms existing baselines in both geometry and appearance reconstruction, particularly for unobserved regions. Moreover, our method naturally supports single-view inputs and unposed videos, with strong generalizability in both indoor and outdoor scenarios with practical real-world applicability. See more results at `https://g4splat.github.io`.

1 INTRODUCTION

Recent advances in 3D Gaussain Splatting (3DGS) (Kerbl et al., 2023) have significantly improved photo-realistic novel view synthesis by enabling efficient 3D scenes reconstruction with dense view

supervision. However, their performance degrades notably in sparsely captured settings due to insufficient geometric and photometric supervision. Depth regularization has been introduced to alleviate this issue (Turkulainen et al., 2025; Li et al., 2024a), but faithful reconstruction remains challenging because of the scale ambiguity inherent in monocular depth estimators (Yang et al., 2024). In addition, these methods are ineffective in under-constrained areas (*i.e.*, regions distant from or invisible to the input views), where no additional scene information can be provided.

More recent approaches (Liu et al., 2024d; Bao et al., 2025) leverage generative knowledge from pre-trained diffusion models to generate missing content in under-constrained regions. However, these approaches still struggle to faithfully reconstruct unobserved regions while maintaining consistency in the observed areas, as illustrated in Fig. 1. We identify two main factors underlying these problems. First, lacking reliable geometric supervision, these methods produce poor reconstruction quality even in observed regions with sparse input views, which undermines the geometric basis essential for inpainting unobserved areas. Second, these methods lack effective mechanisms to mitigate multi-view inconsistencies in diffusion model outputs, which lead to degraded scene recovery due to severe shape–appearance ambiguities (Zhang et al., 2020; Zhong et al., 2025).

In this paper, we argue that robust geometry guidance is fundamental to effectively employing the power of generative models and realizing high-quality reconstruction. To this end, we introduce **G4SPLAT**, which first leverages the prevalence of planar structures in man-made environments, consistent with the Manhattan world assumption (Coughlan & Yuille, 1999), to derive scale-accurate geometric constraints. Unlike matching-based methods (Wang et al., 2024; Guédon et al., 2025) that often fail in non-overlapping regions, planar surfaces allow depth extrapolation: a 3D plane can be reliably estimated from partial depth observations and then extended across the entire surface. We leverage this property by aligning global 3D planes to obtain scale-accurate depth in planar regions and linearly adjusting monocular depth for unobserved non-planar regions, resulting in plane-aware depth maps that provide accurate geometric supervision in both observed and unobserved regions.

Beyond establishing improved geometry as the inpainting basis, we further incorporate geometry guidance into the generative refinement loop to alleviate the shape–appearance ambiguities. We begin by constructing a 3D visibility grid with scale-accurate depth, which provides more reliable visibility masks for inpainting compared to the noisy alpha maps. We also search for novel views by leveraging global 3D planes as object proxies, guiding the placement of novel viewpoints to maximize coverage of complete planar structures and thereby providing richer contextual cues for inpainting. Finally, we inpaint the novel views using a video diffusion model (Ma et al., 2025), while leveraging global 3D planes to modulate the color supervision for reducing cross-view conflicts.

Experiments on Replica (Straub et al., 2019), ScanNet++ (Yeshwanth et al., 2023), and DeepBlending (Hedman et al., 2018) demonstrate that our method consistently outperforms all baselines in both geometric and appearance reconstruction, with particularly strong improvements in unobserved regions. Ablation studies further confirm the effectiveness of each proposed component. Moreover, our approach supports reconstruction from casually captured videos or text-generated single images, as illustrated in Figs. 1 and 5, with significant potential in practical downstream applications.

Our main contributions are summarized as follows:

- We propose a novel method that leverages the plane representation to derive scale-accurate geometric constraints, substantially improving 3D scene reconstruction even in unobserved regions.
- We incorporate geometry guidance in the generative pipeline, which improves visibility mask estimation, novel view selection, and multi-view consistency with video diffusion models, yielding reliable and consistent scene completion.
- Extensive experiments demonstrate that our method achieves state-of-the-art performance on multiple datasets, with support for indoor, outdoor, single-view and unposed video reconstruction.

2 RELATED WORK

2.1 SPARSE-VIEW 3DGS

3D Gaussian Splatting (3DGS)(Kerbl et al., 2023; Lu et al., 2024a; Yu et al., 2024c) has demonstrated impressive reconstruction quality and training efficiency, but its performance deteriorates

significantly when trained with only a few input views. To address this limitation, numerous approaches(Kumar & Vats, 2025; Zhang et al., 2024b; Wu et al., 2025b; Hong et al., 2025; Huang et al., 2025b; Xu et al., 2024; Paliwal et al., 2024; Zhao et al., 2024; 2025a; Bao et al., 2024; Liu et al., 2024f; Yin et al., 2024; Xiao et al., 2024; Lu et al., 2024b; Zheng et al., 2025) have been proposed. For example, DNGaussian (Li et al., 2024a) and FSGS (Zhu et al., 2024) incorporate depth regularization to suppress floaters in visible regions; yet, the scale ambiguity inherent in monocular depth estimators (Yang et al., 2024) prevents them from providing reliable geometric supervision. MAtCha (Guédon et al., 2025) attempts to overcome this limitation by introducing scale-accurate depth from structure-from-motion (SfM) methods (Wang et al., 2024; Duisterhof et al., 2025). Nevertheless, it still struggles to reconstruct non-overlapping regions between input views. To address this issue, we propose to leverage the inherent extensibility of plane representations that propagate accurate depth estimates from overlapping regions to non-overlapping or even unobserved regions.

2.2 Generative Prior for 3DGS

Recent studies (Poole et al., 2022; Xiong et al., 2023; Weber et al., 2024; Wu et al., 2024; Liu et al., 2024e; Melas-Kyriazi et al., 2024; Shih et al., 2024; Paul et al., 2024; Cai et al., 2024; Chen et al., 2024b; Yu et al., 2024a; Ni et al., 2025) have demonstrated the effectiveness of leveraging diffusion models (Rombach et al., 2022; Liu et al., 2023) to provide powerful priors for 3D reconstruction. Some methods (Raj et al., 2025; Huang et al., 2025a; Chang et al., 2025) attempt to introduce 3D geometry priors into the reconstruction process. More recent approaches (Liu et al., 2024a;b;d; Zhao et al., 2025b; Gao et al., 2024; Zhou et al., 2025; Bao et al., 2025; Wu et al., 2025a;c; Fischer et al., 2025; Yin et al., 2025; Zhong et al., 2025) further employ video diffusion models (Blattmann et al., 2023; Yu et al., 2024b) to enhance cross-view consistency. However, since these models primarily rely on initial reconstructions to apply their generative power, they still suffer from numerous floating Gaussian artifacts and low-quality 3D geometry in their results, particularly in the inpainted regions, due to insufficient geometric constraints under sparse observations. To address this issue, we first apply scale-accurate depth supervision for both observed and non-observed regions to provide a robust geometric foundation, and integrate geometric guidance throughout the video diffusion models, leading to significantly improved reconstruction of both geometry and appearance.

2.3 Plane Assumption in Reconstruction

The Manhattan-world assumption (Coughlan & Yuille, 1999), and in particular the plane assumption, has been widely adopted in the reconstruction of man-made environments. Several methods (Liu et al., 2024c; Guo et al., 2024; Mazur et al., 2024; Liu et al., 2025b; Pataki et al., 2025) leverage this assumption in SfM and SLAM to improve matching accuracy, while other plane reconstruction approaches (Liu et al., 2019; Agarwala et al., 2022; Xie et al., 2022; Tan et al., 2023; Watson et al., 2024; Ye et al., 2025; Liu et al., 2025a) directly fit a set of planes to model indoor scenes. More recent studies (Guo et al., 2022; Li et al., 2024b; Chen et al., 2024a; Shi et al., 2025) incorporate the plane assumption to optimize 3D neural implicit representations (Mildenhall et al., 2020; Kerbl et al., 2023). For instance, GeoGaussian (Li et al., 2024c) and IndoorGS (Ruan et al., 2025) impose local planar constraints to regulate Gaussian splitting and movement, whereas PlanarSplatting (Tan et al., 2025) reconstructs 3D scenes as planar primitives directly from multi-view images. Different from these methods, our approach leverages the plane assumption to extract scale-accurate depth, which not only provides geometric guidance for optimizing the Gaussian representation but also facilitates the integration of generative prior, ultimately enabling precise scene reconstruction for both planar and non-planar structures across observed and unobserved regions.

3 Method

We propose **G4Splat**, a method that integrates accurate geometry guidance with generative priors to enhance 3D scene reconstruction. We begin by introducing the base model MAtCha (Guédon et al., 2025) and the overall training objective in Section 3.1. Next, we present our plane-aware geometry modeling in Section 3.2, followed by the geometry-guided generative pipeline in Section 3.3. Finally, we describe the overall training strategy in Section 3.4.

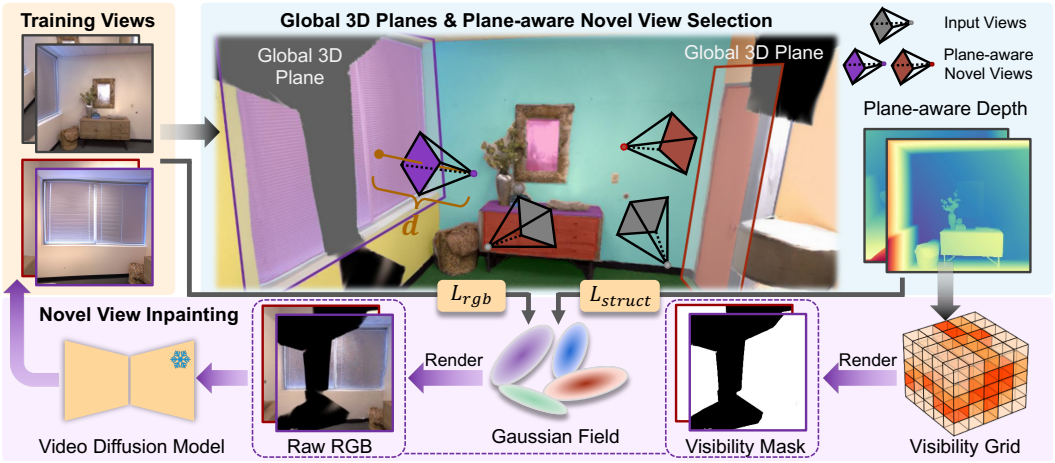

Figure 2: **Overview of G4SPLAT.** For each training loop (Section 3.4), we first extract global 3D planes from all training views and compute plane-aware depth maps (Section 3.2). Subsequently, we construct a visibility grid from these depth maps, select plane-aware novel views, inpaint their invisible regions, and incorporate the completed views back into the training set (Section 3.3).

3.1 BACKGROUND

2D Gaussian Splatting (2DGS) (Huang et al., 2024) extends the original 3D Gaussian Splatting (3DGS) framework (Kerbl et al., 2023) by collapsing 3D volumetric Gaussians into 2D anisotropic disks. Building on 2DGS, MAtCha (Guédon et al., 2025) introduces a chart alignment procedure that optimizes the chart parameters for each input view based on the outputs of MASt3R-SfM (Duisterhof et al., 2025). The chart parameters from all views are then used to generate scale-accurate depth maps, which serve as absolute depth supervision for training 2DGS.

Given N input images $\{I^i\}_{i=1}^N$ with its associated camera poses, the overall training objective of MAtCha combines an RGB reconstruction loss $\mathcal{L}_{\text{rgb}}$, the original 2DGS regularization loss $\mathcal{L}_{\text{reg}}$, and a structure loss $\mathcal{L}_{\text{struct}}$, formulated as:

$$\mathcal{L}_{\text{total}} = \mathcal{L}_{\text{rgb}} + \mathcal{L}_{\text{reg}} + \mathcal{L}_{\text{struct}}. \tag{1}$$

A more detailed description of each term is provided in the Appendix B.3.

However, the effectiveness of chart alignment heavily relies on accurate image correspondences; in regions with poor or missing matches, noticeable errors occur, as shown in Fig. 3a.

3.2 PLANE-AWARE GEOMETRY MODELING

Per-view 2D Plane Extraction Inspired by prior work (Mazur et al., 2024; Ye et al., 2025), we assume that planar regions within an image exhibit consistent normal directions, smooth geometry, and similar semantics. Based on this assumption, we extract plane masks from images by combining normal maps (computed from depth-map gradients or estimated via a monocular normal predictor (Ye et al., 2024)) with instance masks (generated by SAM (Kirillov et al., 2023)). Specifically, we apply K-means clustering to the normal map to obtain regions with coherent surface orientations. These regions are subsequently filtered using SAM masks, and only those assigned the same instance label and exceeding a predefined size threshold are treated as valid 2D plane masks. Example results are shown in Fig. 3a.

Global 3D Plane Estimation The 2D plane masks extracted from individual views are often over-segmented and lack global consistency, resulting in the same 3D plane being fragmented across multiple views. To address this issue, we leverage the 3D scene point cloud to establish correspondences among local masks and merge them into globally consistent 3D planes, as shown in Fig. 3a.

Specifically, for each per-view 2D plane mask, we collect the associated 3D points from the scene point cloud via projection. Two local planes are merged into the same global 3D plane if their associ-

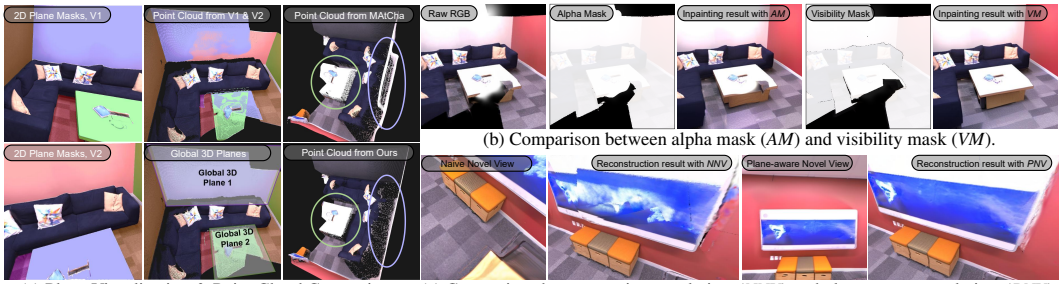

(a) Plane Visualization & Point Cloud Comparison. (b) Comparison between alpha mask (*AM*) and visibility mask (*VM*). (c) Comparison between naive novel view (*NNV*) and plane-aware novel view (*PNV*).

Figure 3: **Visualization of intermediate results.** Our method addresses key issues in prior approaches: (a) MAtCha produces noticeable errors in non-overlapping regions (highlighted by circles); (b) masks derived from alpha maps contain errors in visible areas of novel views; and (c) naive novel view selection offers only local coverage, causing visible seams in the final reconstruction.

ated 3D point sets exhibit sufficient spatial overlap and have similar normal directions. By repeating this process across all views, we obtain a set of global point collections $\{\mathcal{P}_k\}$, each representing a global 3D plane. Further details are in Appendix C.1. Each global 3D plane is represented as:

$$\Phi_k : \mathbf{n}_k^\top \mathbf{x} + d_k = 0, \tag{2}$$

where $\mathbf{n}_k \in \mathbb{R}^3$ is the unit normal vector and $d_k \in \mathbb{R}$ is the offset. To robustly estimate the plane parameters, we select a subset of high-confidence points $\mathcal{P}_k^{\text{conf}} \subset \mathcal{P}_k$, defined as those observed in at least two different views. A 3D plane is then fitted to $\mathcal{P}_k^{\text{conf}}$ by RANSAC (Fischler & Bolles, 1981):

$$\min_{\mathbf{n}_k, d_k} \sum_{\mathbf{p} \in \mathcal{P}_k^{\text{conf}}} (\mathbf{n}_k^\top \mathbf{p} + d_k)^2, \quad \text{s.t. } \|\mathbf{n}_k\| = 1. \tag{3}$$

This procedure produces geometrically accurate and cross-view consistent 3D plane estimates, providing a reliable geometric basis for subsequent optimization.

Plane-Aware Depth Map Extraction With the estimated global 3D planes, we extract a plane-aware depth map D^v for each view v. Let $\{P_i^v\}_{i=1}^M$ denote the set of M 2D plane masks in view v, each associated with a global 3D plane Φ_{k_i}. For each pixel $\mathbf{u} \in P_i^v$, we cast a ray from the camera center $\mathbf{o}^v$ along the ray direction $\mathbf{r}^v(\mathbf{u})$, and compute its depth by intersecting the ray with the global 3D plane Φ_{k_i}:

$$D_i^v(\mathbf{u}) = \frac{-\mathbf{n}_{k_i}^\top \mathbf{o}^v - d_{k_i}}{\mathbf{n}_{k_i}^\top \mathbf{r}^v(\mathbf{u})}. \tag{4}$$

For the non-planar regions of I^v that are visible in the input view, we retain the depth values estimated by MAtCha (Guédon et al., 2025); for those that are not visible, we adopt a pre-trained monocular depth estimator (Yang et al., 2024) to predict a relative depth map $\hat{D}^v$. This relative map is aligned to an absolute scale using the already computed plane region depths $\{D_i^v\}$ via a linear transformation:

$$D^v(\mathbf{u}) = a_v \, \hat{D}^v(\mathbf{u}) + b_v, \tag{5}$$

where the scale a_v and offset b_v are estimated by least-squares fitting over pixels belonging to planar regions. The resulting depth map D^v integrates geometry-consistent plane depths with refined monocular predictions in unobserved non-planar areas, yielding a complete and scale-accurate plane-aware depth representation for each view. As illustrated in Fig. 3a, this plane-aware depth significantly alleviates errors in non-overlapping regions when compared to MAtCha (Guédon et al., 2025).

3.3 Geometry-guided Generative Pipeline

Geometry-Guided Visibility As shown in Fig. 3b, existing methods rely on inpainting masks derived from alpha maps, which often introduce errors within visible regions and thus degrade the inpainting results. To mitigate this issue, we employ scale-accurate plane-aware depth to model

scene visibility using a visibility grid. Specifically, we first determine the 3D boundaries of the scene based on the depth maps from all training views. The scene is then discretized into a voxel grid $\mathcal{G}$. For each voxel, we determine its visibility by projecting its center to each training view and checking whether it falls within the valid depth range. A voxel is marked as visible (*i.e.*, visibility value = 1) if it lies within the observable depth range in at least one view. This visibility assessment is performed in parallel for all voxels, ensuring efficient construction of the visibility grid.

With the visibility grid, we render the visibility map for a novel view using the corresponding GS-rendered depth map. Specifically, pixel-wise visibility is evaluated by casting a ray from the camera center through each pixel and uniformly sampling Q points along the ray up to the rendered depth. The visibility value v_q of each sample point is determined via nearest neighbor interpolation over the visibility grid $\mathcal{G}$. The final per-pixel visibility $V^v(\mathbf{u})$ is computed as

$$V^v(\mathbf{u}) = \prod_{q=1}^{Q} v_q, \tag{6}$$

indicating that a pixel is considered visible only if all Q sampled points along its viewing ray are marked as visible in the visibility grid $\mathcal{G}$.

Plane-Aware Novel View Selection As shown in Fig. 3c, naive novel view selection strategies, such as the elliptical trajectory around the scene center (Wu et al., 2025c), tend to provide only limited local coverage. Inpainting results from these novel views often introduce noticeable artifacts in the final reconstruction due to multiview inconsistencies. To address this issue, we propose a plane-aware view selection strategy that ensures complete coverage of objects for the selected views by leveraging global 3D planes as object proxies. Global 3D planes generally provide sufficient structural and textural cues for object awareness to enable reliable inpainting. For each global 3D plane, we use its centroid as the look-at target and search for a camera center among the visible grid centers in the visibility grid. The selection process is guided by three objectives: maximizing coverage of plane points, minimizing distance to the plane, and encouraging alignment between the viewing direction and the plane normal. More details are described in Appendix C.2.

Geometry-Guided Inpainting For each novel view v, we render the raw RGB map $\tilde{I}^v$ (Eq. A2) along with the visibility mask V^v (Eq. 6). We then employ a pre-trained video diffusion model (Ma et al., 2025), which takes input images as reference $\{I^i\}$, and $\{\tilde{I}^v, V^v\}$ as input to jointly inpaint the occluded regions across all views, producing the completed images $\{\hat{I}^v\}$.

Despite this joint inference, the inpainted results $\{\hat{I}^v\}$ from existing generative models still exhibit multi-view inconsistencies, which can introduce artifacts during training (Zhong et al., 2025). To address this issue, we supervise each region by primarily relying on color information from a single view. For planar regions, we choose the view that provides the most complete observation of the corresponding plane, ensuring consistent inpainting. For non-planar regions, we use the first view in which the region becomes visible, which helps reduce cross-view inconsistencies. A more detailed discussion is provided in Appendix C.3.

3.4 Overall Training Strategy

Our training pipeline consists of two stages: an initialization stage and a geometry-guided generative training loop. This design ensures that reconstruction begins with reliable geometry and progressively improves both coverage and multi-view consistency.

In the initialization stage, we first apply chart alignment in MAtCha to obtain an initial depth map for each input view. From these depth maps, we estimate global 3D planes and compute plane-aware depth maps, as described in Section 3.2. The Gaussian parameters are then initialized from the point cloud of the depth maps and trained with plane-aware depth maps, producing a baseline model with accurate geometry in the regions observed by the input views.

The second stage refines and extends the reconstruction through the iterative process described in Section 3.3. As illustrated in Fig. 2, each loop begins by constructing a visibility grid from the current training views, followed by selecting novel viewpoints and inpainting their invisible regions; the inpainted novel views are then merged into the training set. Subsequently, global 3D planes

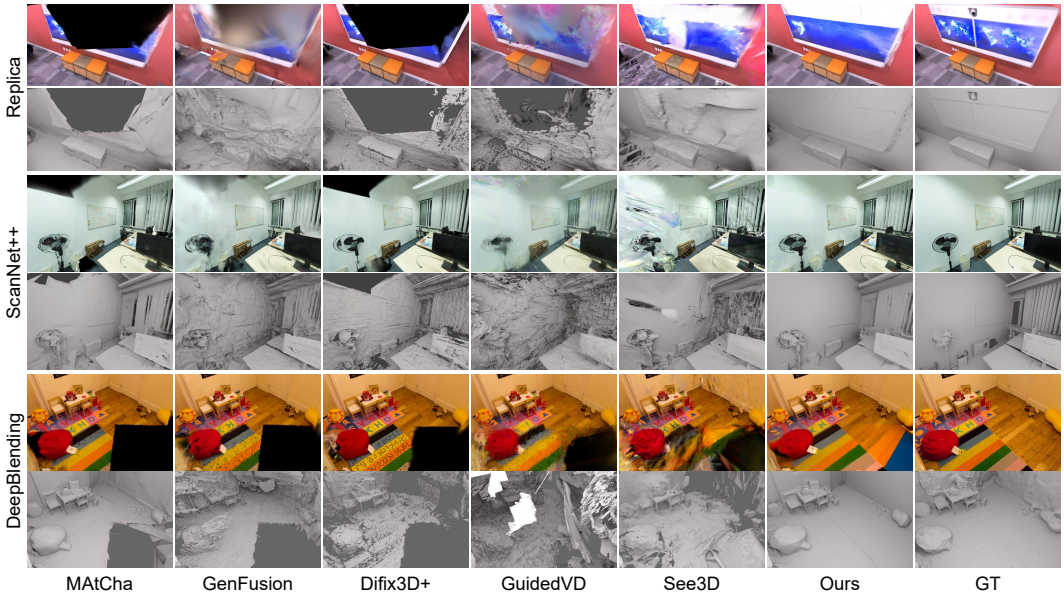

Figure 4: **Qualitative comparison from 5 input views.** Our approach achieves better appearance and geometry reconstruction with fewer Gaussian floaters in both observed and unobserved regions.

and plane-aware depths are recomputed, and the Gaussians are fine-tuned with updated supervision. Repeating this loop progressively recovers unseen regions and corrects geometric misalignments.

During each round of 2DGS training, our method adopts the same total loss formulation as MAtCha (Eq. (1)), but enhances chart depth maps with plane-aware depth maps, thereby introducing stronger geometric constraints that lead to more accurate and consistent reconstructions. In our experiments, we employ three generative training loops; further details are provided in Appendix C.7.

4 Experiments

We evaluate **G4Splat** on both geometric and appearance reconstruction in sparse-view 3D scenarios. Additionally, we present more experimental results in Appendix A, failure cases and discuss the method's limitations in Appendix D. Moreover, video results are available on the anonymous website `https://g4splat.github.io`.

4.1 Settings

Datasets and Metrics We evaluate our method on both synthetic and real-world datasets. The synthetic dataset is Replica (Straub et al., 2019), which contains 8 indoor scenes. The real-world datasets include 6 scenes from ScanNet++(Yeshwanth et al., 2023) and 3 scenes from DeepBlending(Hedman et al., 2018). For quantitative comparisons, we evaluate Chamfer Distance (CD), F-Score, and Normal Consistency (NC) as reconstruction metrics, and PSNR, SSIM, and LPIPS as rendering metrics. More details are provided in Appendices C.5 and C.6.

Baselines We compare our method with several representative baselines. These include the classical Gaussian Splatting approaches 3DGS (Kerbl et al., 2023) and 2DGS (Huang et al., 2024), as well as state-of-the-art sparse-view 3DGS methods FSGS (Zhu et al., 2024), InstantSplat (Fan et al., 2024), and MAtCha (Guédon et al., 2025). We further evaluate against recent approaches that integrate diffusion models into sparse-view 3DGS reconstruction, namely GenFusion (Wu et al., 2025c), Difix3D+ (Wu et al., 2025a) and GuidedVD (Zhong et al., 2025). In addition, we implement a variant of 2DGS augmented with the See3D (Ma et al., 2025). Notably, all baselines are augmented with MASt3R-SfM (Duisterhof et al., 2025) to improve robustness in sparse-view scenarios.

Table 1: **Quantitative comparison from 5 input views.** Our method significantly outperforms all baselines across both reconstruction and rendering metrics. Top-3 results are highlighted as the first, second and third.

Dataset	Method	Reconstruction			Rendering		
		CD↓	F-Score ↑	NC↑	PSNR↑	SSIM↑	LPIPS↓
Replica	3DGS	16.61	27.72	64.34	18.29	0.744	0.254
	2DGS	14.64	48.01	74.14	18.43	0.735	0.306
	FSGS	18.17	26.87	64.16	19.19	0.766	0.259
	InstantSplat	21.00	19.67	62.01	19.39	0.762	0.255
	MAtCha	10.12	60.90	79.33	17.81	0.752	0.228
	See3D	12.74	45.27	73.98	19.22	0.735	0.328
	GenFusion	13.05	41.60	69.33	20.14	0.801	0.258
	Difix3D+	13.71	43.11	65.34	19.42	0.779	0.231
	GuidedVD	27.87	17.29	61.64	22.51	0.822	0.260
	Ours	6.61	65.14	83.98	23.90	0.836	0.199
ScanNet++	3DGS	16.60	31.92	65.35	14.28	0.696	0.372
	2DGS	14.34	51.97	70.01	13.91	0.661	0.429
	FSGS	23.80	27.86	64.53	14.80	0.731	0.362
	InstantSplat	21.32	25.44	60.67	15.02	0.742	0.355
	MAtCha	11.55	62.98	73.61	13.58	0.677	0.351
	See3D	13.03	53.65	70.39	14.76	0.684	0.426
	GenFusion	10.68	47.15	66.27	16.12	0.726	0.347
	Difix3D+	13.15	53.91	67.30	14.09	0.701	0.340
	GuidedVD	25.35	16.67	60.48	17.90	0.807	0.336
	Ours	6.34	67.12	77.45	18.69	0.792	0.314
DeepBlending	3DGS	31.44	20.02	55.39	15.33	0.571	0.489
	2DGS	25.60	23.81	63.82	14.89	0.556	0.506
	FSGS	31.45	19.66	57.38	15.72	0.602	0.476
	InstantSplat	33.78	17.99	57.91	15.00	0.569	0.483
	MAtCha	22.36	26.80	67.92	14.74	0.558	0.465
	See3D	31.34	22.68	63.18	15.00	0.552	0.537
	GenFusion	30.70	22.37	58.70	16.20	0.626	0.468
	Difix3D+	32.70	21.94	58.08	15.18	0.583	0.450
	GuidedVD	43.28	15.95	59.21	16.32	0.618	0.481
	Ours	20.72	28.02	72.04	16.76	0.645	0.440

4.2 Results

Novel View Synthesis Quality By incorporating geometry guidance into the generative prior, our method achieves more accurate renderings in unobserved regions while producing fewer artifacts in observed regions, as illustrated in Figs. 4, A6 and A9 and quantified in Table 1. In contrast, other methods that leverage generative prior exhibit notable limitations. For example, Difix3D+ attains relatively good quality in observed regions but fails to handle unobserved areas. GenFusion, See3D, and GuidedVD can hallucinate content in unobserved regions; however, their completions are blurry and compromised by severe floaters, and they even degrade the reconstruction quality of observed regions. These comparisons highlight the effectiveness of our geometry-guided generative pipeline in maintaining high fidelity across both observed and unobserved regions.

Geometry Reconstruction Quality As shown in Figs. 4, A6 and A9, Difix3D+, GenFusion, See3D and GuidedVD all suffer from severe shape–appearance ambiguities: even when the rendered views appear visually plausible, the reconstructed geometry is of poor quality. In comparison, our approach yields more accurate geometry in unobserved regions and produces smoother, floater-free reconstructions in observed regions. This improvement stems from our plane-aware geometry modeling, which provides reliable depth supervision for both observed and unobserved areas, ensuring consistency across the entire scene. Quantitatively, Table 1 shows that our method significantly outperforms all baselines on all reconstruction metrics across multiple datasets.

Figure 5: **Any-view scene reconstruction.** Our method demonstrates strong generalization across diverse scenarios, including indoor and outdoor scenes, unposed scenes and even single-view scenes.

Any-View Scene Reconstruction As demonstrated in Figs. 1, 5, A1 and A2, our method exhibits robust performance across a wide range of scenarios, including indoor and outdoor scenes, single-view cases and unposed scenes such as YouTube videos. As shown in Table A1, our method consistently outperforms all baselines regardless of the number of input views. Moreover, in scenes with complex lighting, where existing baselines struggle to achieve accurate reconstruction even with dense input views, our approach leverages accurate geometry guidance to effectively suppress errors caused by significant brightness variations across viewpoints, thereby producing high-quality reconstructions, as shown in Fig. A2. In addition to achieving superior results on indoor scenes, as shown in the quantitative and qualitative results on the Mip-NeRF 360 dataset (Table A2 and Fig. A5), our method also outperforms the baselines on outdoor, non-Manhattan, and less structured scenes. Furthermore, the *Museum* in Fig. 1 and the *Cat* in Fig. 5 further demonstrate its capability to handle arbitrary 3D structures.

Table 2: **Ablation study.**

GP	*PM*	*PP*	Reconstruction			Rendering		
			CD↓	F-Score↑	NC↑	PSNR↑	SSIM↑	LPIPS↓
×	×	×	10.60	59.17	79.95	17.85	0.751	0.228
✓	×	×	9.46	56.99	77.58	19.63	0.740	0.295
×	✓	×	8.73	64.96	80.55	17.63	0.752	0.219
✓	✓	×	7.56	62.36	80.89	21.88	0.810	0.221
✓	✓	✓	6.61	65.14	83.98	23.90	0.836	0.199

Table 3: **Running time comparison.**

Method	CD↓	PSNR↑	Time (min)↓
MAtCha	11.57	11.56	32.4
See3D	15.42	14.50	58.6
GenFusion	15.66	16.49	41.4
Difix3D+	17.79	12.94	68.7
GuidedVD	24.29	19.02	141.4
Ours	8.77	20.26	73.3
Ours (DS)	9.33	19.36	43.5

4.3 Ablation Studies

We conduct ablation experiments on Replica dataset to evaluate the contributions of the *generative prior* (*GP*), *plane-aware geometry modeling* (*PM*), and *geometry-guided generative pipeline* (*PP*). As shown in Table 2 and Figs. A7 and A8, we make the following key observations:

1. Incorporating *generative prior* (*GP*) alone improves rendering quality but yields limited gains in geometry reconstruction. LPIPS, F-Score, and NC even decline, as *GP* alone tends to produce averaged, blurry results for the unseen areas. This indicates that directly introducing generative prior fails to perform as expected and leads to shape–appearance ambiguities. Moreover, as shown in Fig. A8, our method is compatible with different generative diffusion models, achieving strong performance across them.
2. Adding *plane-aware geometry modeling* (*PM*), either alone or in combination with *generative prior* (*GP*), significantly improves geometry reconstruction. Moreover, incorporating *PM* along with *GP* brings notable gains in rendering quality. This demonstrates that accurate geometry guidance effectively provides a clean geometry basis and suppresses Gaussian floaters, thereby enabling the generative model to fulfill its intended role.
3. Incorporating *geometry-guided generative pipeline (PP)* further enhances both rendering fidelity and geometric accuracy. This indicates that geometry guidance provides more accurate visibility masks, novel views with broader plane coverage, and consistent color supervision, thereby improving the generative process by mitigating multi-view inconsistencies.

4.4 Discussion on Plane Representation

Our method leverages a plane representation to obtain scale-accurate geometry guidance. We adopt this representation for three main reasons. First, planar structures are common in man-made environments and often occupy a large portion of the image, such as floors, walls, and tabletops. Second, the plane representation exhibits strong generalization. By fitting global 3D planes to accurate point clouds obtained in overlapping regions of input views, we can extend reliable depth estimation to non-overlapping or even unobserved planar regions. The accurate planar depth also enables linear alignment of monocular depth maps, improving depth accuracy of unobserved non-planar regions as well. Finally, the plane representation is simple, computationally efficient, and memory-friendly. As shown in Table 3, our method achieves high-quality reconstruction with a runtime comparable to other approaches that employ generative prior. Moreover, our accelerated variant, *Ours (DS)*, which downsamples the initial Gaussians, substantially reduces runtime while still outperforming all baselines. See additional discussions in Appendices A.2 and C.7.

5 Conclusion

We present **G4Splat**, a geometry-guided generative framework for 3D scene reconstruction. The method first leverages plane representations to derive scale-accurate geometric constraints, and then integrates these constraints throughout the generative pipeline to effectively mitigate shape–appearance ambiguities. Extensive experiments demonstrate that our method consistently outperforms existing approaches in both geometry and appearance reconstruction, with notable improvements in unobserved regions. Moreover, our method naturally supports unposed video and single-view inputs, offering strong potential for practical applications in real-world scenarios.

Reproducibility Statement All experiments were re-run prior to submission to verify the reproducibility and consistency of our results. Comprehensive implementation details and training procedures are provided in the appendix. Upon acceptance, we will make our code, data, and model weights publicly available. The release will include training scripts, evaluation protocols, and thorough documentation to facilitate straightforward reproduction of all experimental results.

REFERENCES

Samir Agarwala, Linyi Jin, Chris Rockwell, and David F Fouhey. Planeformers: From sparse view planes to 3d reconstruction. In *European Conference on Computer Vision (ECCV)*, 2022.

Chong Bao, Xiyu Zhang, Zehao Yu, Jiale Shi, Guofeng Zhang, Songyou Peng, and Zhaopeng Cui. Free360: Layered gaussian splatting for unbounded 360-degree view synthesis from extremely sparse and unposed views. In *Conference on Computer Vision and Pattern Recognition (CVPR)*, 2025.

Zhenyu Bao, Guibiao Liao, Kaichen Zhou, Kanglin Liu, Qing Li, and Guoping Qiu. Loopsparsegs: Loop based sparse-view friendly gaussian splatting. *arXiv preprint arXiv:2408.00254*, 2024.

Andreas Blattmann, Tim Dockhorn, Sumith Kulal, Daniel Mendelevitch, Maciej Kilian, Dominik Lorenz, Yam Levi, Zion English, Vikram Voleti, Adam Letts, et al. Stable video diffusion: Scaling latent video diffusion models to large datasets. *arXiv preprint arXiv:2311.15127*, 2023.

Xudong Cai, Yongcai Wang, Zhaoxin Fan, Deng Haoran, Shuo Wang, Wanting Li, Deying Li, Lun Luo, Minhang Wang, and Jintao Xu. Dust to tower: Coarse-to-fine photo-realistic scene reconstruction from sparse uncalibrated images. *arXiv preprint arXiv:2412.19518*, 2024.

Jiahao Chang, Chongjie Ye, Yushuang Wu, Yuantao Chen, Yidan Zhang, Zhongjin Luo, Chenghong Li, Yihao Zhi, and Xiaoguang Han. Reconviagen: Towards accurate multi-view 3d object reconstruction via generation. *arXiv preprint arXiv:2510.23306*, 2025.

Danpeng Chen, Hai Li, Weicai Ye, Yifan Wang, Weijian Xie, Shangjin Zhai, Nan Wang, Haomin Liu, Hujun Bao, and Guofeng Zhang. Pgsr: Planar-based gaussian splatting for efficient and high-fidelity surface reconstruction. *IEEE Transactions on Visualization and Computer Graphics*, 2024a.

Shen Chen, Jiale Zhou, and Lei Li. Optimizing 3d gaussian splatting for sparse viewpoint scene reconstruction. *arXiv preprint arXiv:2409.03213*, 2024b.

James M Coughlan and Alan L Yuille. Manhattan world: Compass direction from a single image by bayesian inference. In *International Conference on Computer Vision (ICCV)*, 1999.

Bardienus Pieter Duisterhof, Lojze Zust, Philippe Weinzaepfel, Vincent Leroy, Yohann Cabon, and Jerome Revaud. MASt3r-sfm: a fully-integrated solution for unconstrained structure-from-motion. In *International Conference on 3D Vision (3DV)*, 2025.

Patrick Esser, Sumith Kulal, Andreas Blattmann, Rahim Entezari, Jonas Müller, Harry Saini, Yam Levi, Dominik Lorenz, Axel Sauer, Frederic Boesel, et al. Scaling rectified flow transformers for high-resolution image synthesis. In *International Conference on Machine Learning (ICML)*, 2024.

Zhiwen Fan, Kairun Wen, Wenyan Cong, Kevin Wang, Jian Zhang, Xinghao Ding, Danfei Xu, Boris Ivanovic, Marco Pavone, Georgios Pavlakos, Zhangyang Wang, and Yue Wang. Instantsplat: Sparse-view gaussian splatting in seconds. *arXiv preprint arXiv:2403.20309*, 2024.

Tobias Fischer, Samuel Rota Bulò, Yung-Hsu Yang, Nikhil Keetha, Lorenzo Porzi, Norman Müller, Katja Schwarz, Jonathon Luiten, Marc Pollefeys, and Peter Kontschieder. FlowR: Flowing from sparse to dense 3d reconstructions. In *International Conference on Computer Vision (ICCV)*, 2025.

Martin A. Fischler and Robert C. Bolles. Random sample consensus: a paradigm for model fitting with applications to image analysis and automated cartography. *Commun. ACM*, 1981.

Ruiqi Gao, Aleksander Holynski, Philipp Henzler, Arthur Brussee, Ricardo Martin-Brualla, Pratul P. Srinivasan, Jonathan T. Barron, and Ben Poole. Cat3d: Create anything in 3d with multi-view diffusion models. In *Advances in Neural Information Processing Systems (NeurIPS)*, 2024.

Antoine Guédon, Tomoki Ichikawa, Kohei Yamashita, and Ko Nishino. Matcha gaussians: Atlas of charts for high-quality geometry and photorealism from sparse views. In *Conference on Computer Vision and Pattern Recognition (CVPR)*, 2025.

Haoyu Guo, Sida Peng, Haotong Lin, Qianqian Wang, Guofeng Zhang, Hujun Bao, and Xiaowei Zhou. Neural 3d scene reconstruction with the manhattan-world assumption. In *Conference on Computer Vision and Pattern Recognition (CVPR)*, 2022.

Haoyu Guo, Sida Peng, Ting Shen, and Xiaowei Zhou. Planestereo: Plane-aware multi-view stereo. *Machine Intelligence Research*, 2024.

Peter Hedman, Julien Philip, True Price, Jan-Michael Frahm, George Drettakis, and Gabriel Brostow. Deep blending for free-viewpoint image-based rendering. *ACM Transactions on Graphics (ToG)*, 2018.

Yuhang Hong, Bo Tao, and Zeyu Gong. Sharegs: Hole completion with sparse inputs based on reusing selected scene information. *Pattern Recognition*, 2025.

Binbin Huang, Zehao Yu, Anpei Chen, Andreas Geiger, and Shenghua Gao. 2d gaussian splatting for geometrically accurate radiance fields. In *ACM SIGGRAPH / Eurographics Symposium on Computer Animation (SCA)*, 2024.

Binbin Huang, Haobin Duan, Yiqun Zhao, Zibo Zhao, Yi Ma, and Shenghua Gao. Cupid: Pose-grounded generative 3d reconstruction from a single image. *arXiv preprint arXiv:2510.20776*, 2025a.

Han Huang, Yulun Wu, Chao Deng, Ge Gao, Ming Gu, and Yu-Shen Liu. Fatesgs: Fast and accurate sparse-view surface reconstruction using gaussian splatting with depth-feature consistency. In *AAAI Conference on Artificial Intelligence (AAAI)*, 2025b.

Bernhard Kerbl, Georgios Kopanas, Thomas Leimkühler, and George Drettakis. 3d gaussian splatting for real-time radiance field rendering. In *ACM SIGGRAPH / Eurographics Symposium on Computer Animation (SCA)*, 2023.

Alexander Kirillov, Eric Mintun, Nikhila Ravi, Hanzi Mao, Chloe Rolland, Laura Gustafson, Tete Xiao, Spencer Whitehead, Alexander C. Berg, Wan-Yen Lo, Piotr Dollár, and Ross Girshick. Segment anything. In *International Conference on Computer Vision (ICCV)*, 2023.

Jonas Kulhanek, Songyou Peng, Zuzana Kukelova, Marc Pollefeys, and Torsten Sattler. WildGaussians: 3D gaussian splatting in the wild. In *Advances in Neural Information Processing Systems (NeurIPS)*, 2024.

Raja Kumar and Vanshika Vats. Few-shot novel view synthesis using depth aware 3d gaussian splatting. In *European Conference on Computer Vision Workshop*, 2025.

Jiahe Li, Jiawei Zhang, Xiao Bai, Jin Zheng, Xin Ning, Jun Zhou, and Lin Gu. Dngaussian: Optimizing sparse-view 3d gaussian radiance fields with global-local depth normalization. In *Conference on Computer Vision and Pattern Recognition (CVPR)*, 2024a.

Jing Li, Jinpeng Yu, Ruoyu Wang, and Shenghua Gao. Pseudo-plane regularized signed distance field for neural indoor scene reconstruction. *International Journal of Computer Vision (IJCV)*, 2024b.

Yanyan Li, Chenyu Lyu, Yan Di, Guangyao Zhai, Gim Hee Lee, and Federico Tombari. Geogaussian: Geometry-aware gaussian splatting for scene rendering. In *European Conference on Computer Vision (ECCV)*, 2024c.

Chen Liu, Kihwan Kim, Jinwei Gu, Yasutaka Furukawa, and Jan Kautz. Planercnn: 3d plane detection and reconstruction from a single image. In *Conference on Computer Vision and Pattern Recognition (CVPR)*, 2019.

Fangfu Liu, Wenqiang Sun, Hanyang Wang, Yikai Wang, Haowen Sun, Junliang Ye, Jun Zhang, and Yueqi Duan. Reconx: Reconstruct any scene from sparse views with video diffusion model. *arXiv preprint arXiv:2408.16767*, 2024a.

Jiachen Liu, Rui Yu, Sili Chen, Sharon X Huang, and Hengkai Guo. Towards in-the-wild 3d plane reconstruction from a single image. In *Conference on Computer Vision and Pattern Recognition (CVPR)*, 2025a.

Kunhao Liu, Ling Shao, and Shijian Lu. Novel view extrapolation with video diffusion priors. *arXiv preprint arXiv:2411.14208*, 2024b.

Ruoshi Liu, Rundi Wu, Basile Van Hoorick, Pavel Tokmakov, Sergey Zakharov, and Carl Vondrick. Zero-1-to-3: Zero-shot one image to 3d object. In *International Conference on Computer Vision (ICCV)*, 2023.

Shuhong Liu, Heng Zhou, Liuzhuozheng Li, Yun Liu, Tianchen Deng, Yiming Zhou, and Mingrui Li. Structure gaussian slam with manhattan world hypothesis. *arXiv preprint arXiv:2405.20031*, 2024c.

Shuhong Liu, Tianchen Deng, Heng Zhou, Liuzhuozheng Li, Hongyu Wang, Danwei Wang, and Mingrui Li. Mg-slam: Structure gaussian splatting slam with manhattan world hypothesis. *IEEE Transactions on Automation Science and Engineering*, 2025b.

Xi Liu, Chaoyi Zhou, and Siyu Huang. 3dgs-enhancer: Enhancing unbounded 3d gaussian splatting with view-consistent 2d diffusion priors. In *Advances in Neural Information Processing Systems (NeurIPS)*, 2024d.

Xinhang Liu, Jiaben Chen, Shiu-hong Kao, Yu-Wing Tai, and Chi-Keung Tang. Deceptive-nerf/3dgs: Diffusion-generated pseudo-observations for high-quality sparse-view reconstruction. In *European Conference on Computer Vision (ECCV)*, 2024e.

Zhaoliang Liu, Jinhe Su, Guorong Cai, Yidong Chen, Binghui Zeng, and Zongyue Wang. Georgs: Geometric regularization for real-time novel view synthesis from sparse inputs. *IEEE Transactions on Circuits and Systems for Video Technology*, 2024f.

Tao Lu, Mulin Yu, Linning Xu, Yuanbo Xiangli, Limin Wang, Dahua Lin, and Bo Dai. Scaffold-gs: Structured 3d gaussians for view-adaptive rendering. In *Conference on Computer Vision and Pattern Recognition (CVPR)*, 2024a.

Ziqi Lu, Heng Yang, Danfei Xu, Boyi Li, Boris Ivanovic, Marco Pavone, and Yue Wang. Lora3d: Low-rank self-calibration of 3d geometric foundation models. In *International Conference on Learning Representations (ICLR)*, 2024b.

Baorui Ma, Huachen Gao, Haoge Deng, Zhengxiong Luo, Tiejun Huang, Lulu Tang, and Xinlong Wang. You see it, you got it: Learning 3d creation on pose-free videos at scale. In *Conference on Computer Vision and Pattern Recognition (CVPR)*, 2025.

Kirill Mazur, Gwangbin Bae, and Andrew Davison. Superprimitive: Scene reconstruction at a primitive level. In *Conference on Computer Vision and Pattern Recognition (CVPR)*, 2024.

Luke Melas-Kyriazi, Iro Laina, Christian Rupprecht, Natalia Neverova, Andrea Vedaldi, Oran Gafni, and Filippos Kokkinos. Im-3d: Iterative multiview diffusion and reconstruction for high-quality 3d generation. In *International Conference on Machine Learning (ICML)*, 2024.

Ben Mildenhall, Pratul P. Srinivasan, Matthew Tancik, Jonathan T. Barron, Ravi Ramamoorthi, and Ren Ng. Nerf: Representing scenes as neural radiance fields for view synthesis. In *European Conference on Computer Vision (ECCV)*, 2020.

Junfeng Ni, Yu Liu, Ruijie Lu, Zirui Zhou, Song-Chun Zhu, Yixin Chen, and Siyuan Huang. Decompositional neural scene reconstruction with generative diffusion prior. In *Conference on Computer Vision and Pattern Recognition (CVPR)*, 2025.

Avinash Paliwal, Wei Ye, Jinhui Xiong, Dmytro Kotovenko, Rakesh Ranjan, Vikas Chandra, and Nima Khademi Kalantari. Coherentgs: Sparse novel view synthesis with coherent 3d gaussians. In *European Conference on Computer Vision (ECCV)*, 2024.

Adam Paszke, Sam Gross, Francisco Massa, Adam Lerer, James Bradbury, Gregory Chanan, Trevor Killeen, Zeming Lin, Natalia Gimelshein, Luca Antiga, et al. Pytorch: An imperative style, high-performance deep learning library. In *Advances in Neural Information Processing Systems (NeurIPS)*, 2019.

Zador Pataki, Paul-Edouard Sarlin, Johannes L Schönberger, and Marc Pollefeys. Mp-sfm: Monocular surface priors for robust structure-from-motion. In *Conference on Computer Vision and Pattern Recognition (CVPR)*, 2025.

Soumava Paul, Prakhar Kaushik, and Alan Yuille. Gaussian scenes: Pose-free sparse-view scene reconstruction using depth-enhanced diffusion priors. *arXiv preprint arXiv:2411.15966*, 2024.

Ben Poole, Ajay Jain, Jonathan T. Barron, and Ben Mildenhall. Dreamfusion: Text-to-3d using 2d diffusion. In *International Conference on Learning Representations (ICLR)*, 2022.

Kevin Raj, Christopher Wewer, Raza Yunus, Eddy Ilg, and Jan Eric Lenssen. Spurfies: Sparse-view surface reconstruction using local geometry priors. In *International Conference on 3D Vision 2025*, 2025.

Robin Rombach, Andreas Blattmann, Dominik Lorenz, Patrick Esser, and Björn Ommer. High-resolution image synthesis with latent diffusion models. In *Conference on Computer Vision and Pattern Recognition (CVPR)*, 2022.

Cong Ruan, Yuesong Wang, Tao Guan, Bin Zhang, and Lili Ju. Indoorgs: Geometric cues guided gaussian splatting for indoor scene reconstruction. In *Conference on Computer Vision and Pattern Recognition (CVPR)*, 2025.

Kyle Sargent, Zizhang Li, Tanmay Shah, Charles Herrmann, Hong-Xing Yu, Yunzhi Zhang, Eric Ryan Chan, Dmitry Lagun, Li Fei-Fei, Deqing Sun, et al. Zeronvs: Zero-shot 360-degree view synthesis from a single image. In *Conference on Computer Vision and Pattern Recognition (CVPR)*, 2024.

Yuang Shi, Simone Gasparini, Géraldine Morin, Chenggang Yang, and Wei Tsang Ooi. Sketch and patch: Efficient 3d gaussian representation for man-made scenes. In *Proceedings of the 17th International Workshop on IMmersive Mixed and Virtual Environment Systems*, 2025.

Meng-Li Shih, Wei-Chiu Ma, Lorenzo Boyice, Aleksander Holynski, Forrester Cole, Brian L. Curless, and Janne Kontkanen. Extranerf: Visibility-aware view extrapolation of neural radiance fields with diffusion models. In *Conference on Computer Vision and Pattern Recognition (CVPR)*, 2024.

Karen Simonyan and Andrew Zisserman. Very deep convolutional networks for large-scale image recognition. *arXiv preprint arXiv:1409.1556*, 2014.

Julian Straub, Thomas Whelan, Lingni Ma, Yufan Chen, Erik Wijmans, Simon Green, Jakob J. Engel, Raul Mur-Artal, Carl Ren, Shobhit Verma, Anton Clarkson, Mingfei Yan, Brian Budge, Yajie Yan, Xiaqing Pan, June Yon, Yuyang Zou, Kimberly Leon, Nigel Carter, Jesus Briales, Tyler Gillingham, Elias Mueggler, Luis Pesqueira, Manolis Savva, Dhruv Batra, Hauke M. Strasdat, Renzo De Nardi, Michael Goesele, Steven Lovegrove, and Richard Newcombe. The Replica dataset: A digital replica of indoor spaces. *arXiv preprint arXiv:1906.05797*, 2019.

Bin Tan, Nan Xue, Tianfu Wu, and Gui-Song Xia. Nope-sac: Neural one-plane ransac for sparse-view planar 3d reconstruction. *Transactions on Pattern Analysis and Machine Intelligence (TPAMI)*, 2023.

Bin Tan, Rui Yu, Yujun Shen, and Nan Xue. Planarsplatting: Accurate planar surface reconstruction in 3 minutes. In *Conference on Computer Vision and Pattern Recognition (CVPR)*, 2025.

Matias Turkulainen, Xuqian Ren, Iaroslav Melekhov, Otto Seiskari, Esa Rahtu, and Juho Kannala. Dn-splatter: Depth and normal priors for gaussian splatting and meshing. In *Proceedings of Winter Conference on Applications of Computer Vision (WACV)*, 2025.

Shuzhe Wang, Vincent Leroy, Yohann Cabon, Boris Chidlovskii, and Jerome Revaud. Dust3r: Geometric 3d vision made easy. In *Conference on Computer Vision and Pattern Recognition (CVPR)*, 2024.

Jamie Watson, Filippo Aleotti, Mohamed Sayed, Zawar Qureshi, Oisin Mac Aodha, Gabriel Brostow, Michael Firman, and Sara Vicente. Airplanes: Accurate plane estimation via 3d-consistent embeddings. In *Conference on Computer Vision and Pattern Recognition (CVPR)*, 2024.

Ethan Weber, Aleksander Holynski, Varun Jampani, Saurabh Saxena, Noah Snavely, Abhishek Kar, and Angjoo Kanazawa. Nerfiller: Completing scenes via generative 3d inpainting. In *Conference on Computer Vision and Pattern Recognition (CVPR)*, 2024.

Jay Zhangjie Wu, Yuxuan Zhang, Haithem Turki, Xuanchi Ren, Jun Gao, Mike Zheng Shou, Sanja Fidler, Zan Gojcic, and Huan Ling. Difix3d+: Improving 3d reconstructions with single-step diffusion models. In *Conference on Computer Vision and Pattern Recognition (CVPR)*, 2025a.

Jiang Wu, Rui Li, Yu Zhu, Rong Guo, Jinqiu Sun, and Yanning Zhang. Sparse2dgs: Geometry-prioritized gaussian splatting for surface reconstruction from sparse views. In *Conference on Computer Vision and Pattern Recognition (CVPR)*, 2025b.

Rundi Wu, Ben Mildenhall, Philipp Henzler, Keunhong Park, Ruiqi Gao, Daniel Watson, Pratul P. Srinivasan, Dor Verbin, Jonathan T. Barron, Ben Poole, and Aleksander Holynski. Reconfusion: 3d reconstruction with diffusion priors. In *Conference on Computer Vision and Pattern Recognition (CVPR)*, 2024.

Sibo Wu, Congrong Xu, Binbin Huang, Geiger Andreas, and Anpei Chen. Genfusion: Closing the loop between reconstruction and generation via videos. In *Conference on Computer Vision and Pattern Recognition (CVPR)*, 2025c.

Yuru Xiao, Deming Zhai, Wenbo Zhao, Kui Jiang, Junjun Jiang, and Xianming Liu. Mcgs: Multiview consistency enhancement for sparse-view 3d gaussian radiance fields. *arXiv preprint arXiv:2410.11394*, 2024.

Yiming Xie, Matheus Gadelha, Fengting Yang, Xiaowei Zhou, and Huaizu Jiang. Planarrecon: Real-time 3d plane detection and reconstruction from posed monocular videos. In *Conference on Computer Vision and Pattern Recognition (CVPR)*, 2022.

Haolin Xiong, Sairisheek Muttukuru, Rishi Upadhyay, Pradyumna Chari, and Achuta Kadambi. Sparsegs: Real-time 360° sparse view synthesis using gaussian splatting. *arXiv preprint arXiv:2312.00206*, 2023.

Wangze Xu, Huachen Gao, Shihe Shen, Rui Peng, Jianbo Jiao, and Ronggang Wang. Mvpgs: Excavating multi-view priors for gaussian splatting from sparse input views. In *European Conference on Computer Vision (ECCV)*, 2024.

Lihe Yang, Bingyi Kang, Zilong Huang, Zhen Zhao, Xiaogang Xu, Jiashi Feng, and Hengshuang Zhao. Depth anything v2. In *Advances in Neural Information Processing Systems (NeurIPS)*, 2024.

Zesong Yang, Bangbang Yang, Wenqi Dong, Chenxuan Cao, Liyuan Cui, Yuewen Ma, Zhaopeng Cui, and Hujun Bao. Instascene: Towards complete 3d instance decomposition and reconstruction from cluttered scenes. In *International Conference on Computer Vision (ICCV)*, 2025.

Chongjie Ye, Lingteng Qiu, Xiaodong Gu, Qi Zuo, Yushuang Wu, Zilong Dong, Liefeng Bo, Yuliang Xiu, and Xiaoguang Han. Stablenormal: Reducing diffusion variance for stable and sharp normal. *ACM Transactions on Graphics (TOG)*, 2024.

Hanqiao Ye, Yuzhou Liu, Yangdong Liu, and Shuhan Shen. Neuralplane: Structured 3d reconstruction in planar primitives with neural fields. In *International Conference on Learning Representations (ICLR)*, 2025.

Chandan Yeshwanth, Yueh-Cheng Liu, Matthias Nießner, and Angela Dai. Scannet++: A high-fidelity dataset of 3d indoor scenes. In *International Conference on Computer Vision (ICCV)*, 2023.

Ruihong Yin, Vladimir Yugay, Yue Li, Sezer Karaoglu, and Theo Gevers. Fewviewgs: Gaussian splatting with few view matching and multi-stage training. In *Advances in Neural Information Processing Systems (NeurIPS)*, 2024.

Xingyilang Yin, Qi Zhang, Jiahao Chang, Ying Feng, Qingnan Fan, Xi Yang, Chi-Man Pun, Huaqi Zhang, and Xiaodong Cun. Gsfixer: Improving 3d gaussian splatting with reference-guided video diffusion priors. *arXiv preprint arXiv:2508.09667*, 2025.

Hanyang Yu, Xiaoxiao Long, and Ping Tan. Lm-gaussian: Boost sparse-view 3d gaussian splatting with large model priors. *arXiv preprint arXiv:2409.03456*, 2024a.

Wangbo Yu, Jinbo Xing, Li Yuan, Wenbo Hu, Xiaoyu Li, Zhipeng Huang, Xiangjun Gao, Tien-Tsin Wong, Ying Shan, and Yonghong Tian. Viewcrafter: Taming video diffusion models for high-fidelity novel view synthesis. *arXiv preprint arXiv:2409.02048*, 2024b.

Zehao Yu, Songyou Peng, Michael Niemeyer, Torsten Sattler, and Andreas Geiger. Monosdf: Exploring monocular geometric cues for neural implicit surface reconstruction. In *Advances in Neural Information Processing Systems (NeurIPS)*, 2022.

Zehao Yu, Anpei Chen, Binbin Huang, Torsten Sattler, and Andreas Geiger. Mip-splatting: Alias-free 3d gaussian splatting. In *Conference on Computer Vision and Pattern Recognition (CVPR)*, 2024c.

Dongbin Zhang, Chuming Wang, Weitao Wang, Peihao Li, Minghan Qin, and Haoqian Wang. Gaussian in the wild: 3d gaussian splatting for unconstrained image collections. In *European Conference on Computer Vision (ECCV)*, 2024a.

Jiawei Zhang, Jiahe Li, Xiaohan Yu, Lei Huang, Lin Gu, Jin Zheng, and Xiao Bai. Cor-gs: Sparse-view 3d gaussian splatting via co-regularization. In *European Conference on Computer Vision (ECCV)*, 2024b.

Kai Zhang, Gernot Riegler, Noah Snavely, and Vladlen Koltun. Nerf++: Analyzing and improving neural radiance fields. *arXiv preprint arXiv:2010.07492*, 2020.

Chen Zhao, Xuan Wang, Tong Zhang, Saqib Javed, and Mathieu Salzmann. Self-ensembling gaussian splatting for few-shot novel view synthesis. In *International Conference on Computer Vision (ICCV)*, 2025a.

Liang Zhao, Zehan Bao, Yi Xie, Hong Chen, Yaohui Chen, and Weifu Li. Tsgaussian: Semantic and depth-guided target-specific gaussian splatting from sparse views. *arXiv preprint arXiv:2412.10051*, 2024.

Yuyang Zhao, Chung-Ching Lin, Kevin Lin, Zhiwen Yan, Linjie Li, Zhengyuan Yang, Jianfeng Wang, Gim Hee Lee, and Lijuan Wang. Genxd: Generating any 3d and 4d scenes. In *International Conference on Learning Representations (ICLR)*, 2025b.

Yulong Zheng, Zicheng Jiang, Shengfeng He, Yandu Sun, Junyu Dong, Huaidong Zhang, and Yong Du. Nexusgs: Sparse view synthesis with epipolar depth priors in 3d gaussian splatting. In *Conference on Computer Vision and Pattern Recognition (CVPR)*, 2025.

Yingji Zhong, Zhihao Li, Dave Zhenyu Chen, Lanqing Hong, and Dan Xu. Taming video diffusion prior with scene-grounding guidance for 3d gaussian splatting from sparse inputs. In *Conference on Computer Vision and Pattern Recognition (CVPR)*, 2025.

Jensen (Jinghao) Zhou, Hang Gao, Vikram Voleti, Aaryaman Vasishta, Chun-Han Yao, Mark Boss, Philip Torr, Christian Rupprecht, and Varun Jampani. Stable virtual camera: Generative view synthesis with diffusion models. *arXiv preprint arXiv:2503.14489*, 2025.

Zehao Zhu, Zhiwen Fan, Yifan Jiang, and Zhangyang Wang. Fsgs: Real-time few-shot view synthesis using gaussian splatting. In *European Conference on Computer Vision (ECCV)*, 2024.

APPENDIX

This appendix provides additional details and analyses that complement the main paper. Appendix A presents extended experimental results, including single-view and dense-view reconstruction experiments, performance under varying numbers of input views, and additional qualitative results. Appendix B offers further background information on our approach. Appendix C describes additional training and implementation details to facilitate reproducibility. Appendix D discusses typical failure cases and limitations of our method. Finally, Appendix E provides a statement on the usage of large language models (LLMs) during the development of this work. In addition, video results are available at the anonymous website `https://g4splat.github.io`, and the corresponding video files are also included in the supplementary materials.

A MORE EXPERIMENT RESULTS

A.1 SINGLE-VIEW RECONSTRUCTION

For the single-view reconstruction experiment, we use an image generated by a text-to-image model (Esser et al., 2024) as input. We observe that inpainting-based video diffusion models, such as See3D (Ma et al., 2025), are less effective at synthesizing large unseen regions in a scene when only a single reference view is available. In contrast, camera-control video diffusion models like Stable Virtual Camera (Zhou et al., 2025) perform significantly better in this setting. A more detailed discussion on the choice of generative models is provided in Appendix C.4. Based on these observations, we adopt Stable Virtual Camera as the generative prior in our method: it is first employed to generate multiple novel views conditioned on the input single-view image, and these views are then used to train our model. Additional single-view reconstruction results are shown in Fig. A1.

Figure A1: **More results of single-view reconstruction.** Our method achieves high-quality geometry reconstruction (*i.e.*, geometry view) and realistic texture recovery (*i.e.*, appearance view). The appearance view is obtained by rendering the exported colored mesh in Blender.

A.2 DENSE-VIEW RECONSTRUCTION

Our method not only outperforms the baselines under the sparse-view setting, but also achieves superior results when dense input views are available. Methods based on Gaussian Splatting often struggle to reconstruct regions with strong specularities and reflections in scenes with complex lighting (Zhang et al., 2024a; Kulhanek et al., 2024). This difficulty arises because the color in such regions varies significantly across different viewpoints, making it challenging for explicit representations like Gaussian to fit them. In contrast, by incorporating scale-accurate geometry supervision, our approach effectively mitigates large color variations across views and produces accurate geometry reconstructions. As shown in Fig. A2, for a scene with 383 input views, our reconstruction results are substantially better than those of the baselines.

Although MAtCha can obtain reasonable depth supervision in chart views through chart alignment, it requires maintaining a separate chart representation for each chart view during the alignment process, as introduced in Appendix B.2. This results in high memory consumption, allowing only

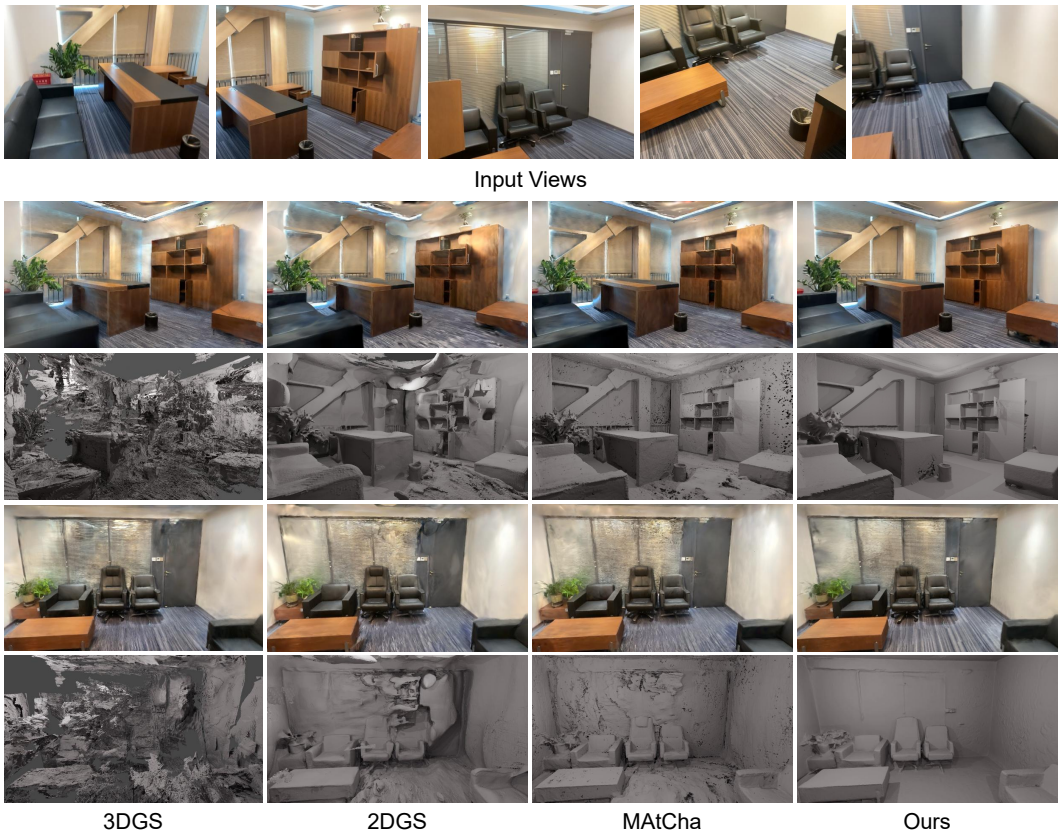

Figure A2: **Dense view reconstruction comparison.**

about 20 chart representations to be maintained on an NVIDIA 3090 GPU. In contrast, our method leverages global 3D planes, each stored compactly as a plane equation $(\mathbf{n}_k, d_k)$, which requires minimal memory overhead. Moreover, since all computations are based on projections, our approach can efficiently obtain scale-accurate depths for all input views by exploiting CUDA parallelization. All methods in Fig. A2 are evaluated on a single NVIDIA 3090 GPU.

A.3 Performance under Different Numbers of Views

We further assess the robustness of our method under varying numbers of input views. As summarized in Table A1, our approach consistently outperforms all baselines in both rendering quality and geometric accuracy, regardless of the number of input views. In particular, Fig. A2 illustrates that our method achieves markedly superior results when dense views are available, while Fig. A1 demonstrates that it still delivers strong reconstructions even with a single input view. These results highlight the effectiveness and generalizability of our design across diverse input-view scenarios.

A.4 More Qualitative Results

Additional qualitative results are presented in Fig. A9. These results further demonstrate that combining geometry guidance with the generative prior effectively alleviates shape–appearance ambiguities, leading to significant improvements in both geometry reconstruction and rendering quality, particularly in regions that are unobserved by the input views.

Table A1: **Quantitative results on varying numbers of input views in the Replica dataset.** Our method consistently outperforms baselines regardless of the number of input views.

	Reconstruction (CD↓ / NC↑)			Rendering (PSNR↑/LPIPS↓)		
Method	5 views	10 views	15 views	5 views	10 views	15 views
2DGS	14.64 / 74.14	9.37 / 81.24	7.17 / 85.33	18.43 / 0.306	21.79 / 0.207	25.30 / 0.139
FSGS	18.17 / 64.16	13.97 / 68.76	12.64 / 71.22	19.19 / 0.259	22.50 / 0.179	25.84 / 0.127
MAtCha	11.10 / 81.20	7.35 / 83.99	6.03 / 85.67	17.85 / 0.228	21.26 / 0.153	25.00 / 0.109
See3D	12.74 / 73.98	9.22 / 80.44	7.40 / 84.22	19.22 / 0.328	22.73 / 0.240	25.56 / 0.183
GenFusion	13.05 / 69.33	10.04 / 74.03	8.88 / 76.57	20.14 / 0.258	23.90 / 0.183	26.48 / 0.138
Difix3D+	13.71 / 65.34	10.15 / 68.43	7.97 / 70.73	19.42 / 0.231	22.68 / 0.165	26.04 / 0.122
GuidedVD	27.87 / 61.64	20.30 / 64.53	16.62 / 68.54	22.51 / 0.260	25.63 / 0.205	27.91 / 0.163
Ours	6.61 / 83.98	4.88 / 85.49	3.98 / 87.25	23.90 / 0.199	27.48 / 0.140	30.22 / 0.094

B Background

B.1 Alpha Rendering in 2DGS

In 2DGS (Huang et al., 2024), the value at a point $\mathbf{u} = (u, v)$ within the disk of a 2D Gaussian is defined by the Gaussian function:

$$g(\mathbf{u}) = \exp\left(-\frac{u^2 + v^2}{2}\right). \tag{A1}$$

Each 2D Gaussian is associated with an opacity α and a view-dependent color $\mathbf{c}$ represented using spherical harmonics. During rasterization, Gaussians are depth-sorted and composited into the final image using front-to-back alpha blending:

$$\mathbf{c}(\mathbf{x}) = \sum_{i=1}^{N} \mathbf{c}_i \alpha_i g_i\big(\mathbf{u}(\mathbf{x})\big) \prod_{j=1}^{i-1} \big[1 - \alpha_j g_j\big(\mathbf{u}(\mathbf{x})\big)\big], \tag{A2}$$

where $\mathbf{u}(\mathbf{x})$ denotes the (u, v) coordinate obtained by intersecting the camera ray through pixel $\mathbf{x}$ with the corresponding 2D Gaussian disk.

Similarly, the depth map can be computed in the same manner, by replacing colors with the z-buffer values of the corresponding Gaussians.

$$d(\mathbf{x}) = \sum_{i=1}^{N} d_i \alpha_i g_i\big(\mathbf{u}(\mathbf{x})\big) \prod_{j=1}^{i-1} \big[1 - \alpha_j g_j\big(\mathbf{u}(\mathbf{x})\big)\big], \tag{A3}$$

where d_i represents the z-buffer value of the i-th 2D Gaussian disk.

B.2 Chart Representation and Alignment in MAtCha

MAtCha (Guédon et al., 2025) represents each chart with a lightweight deformation model designed to balance flexibility and efficiency. Each chart is parameterized by a sparse 2D grid of learnable features in UV space, together with a small MLP that maps these features to 3D deformation vectors. To properly handle depth discontinuities across object boundaries, the model is further augmented with depth-dependent features, allowing points at different depths to be deformed independently, even if they are close in UV space. This design preserves high-frequency details from the initial charts while capturing low-frequency, object-dependent deformations.

Each chart is initialized from a monocular depth map estimated by a monocular depth predictor (Yang et al., 2024). To ensure geometric consistency across views, MAtCha then performs an alignment stage that jointly optimizes chart deformations under multiple objectives.

Fitting loss To align charts with sparse SfM points, MAtCha minimizes their distances to the deformed charts:

$$\mathcal{L}_{\text{fit}} = \frac{1}{n} \sum_{i=0}^{n-1} \sum_{k=0}^{m_i-1} C_i(u_{ik}) \|\psi_i(u_{ik}) - p_{ik}\|_1 - \alpha \sum_{i=0}^{n-1} \log(C_i)\,, \tag{A4}$$

where $\psi_i(u)$ denotes the deformed 3D position of UV coordinate u on chart i, and p_{ik} is the 3D position of the k-th SfM point visible in image i. The confidence map C_i is learnable and downweights unreliable SfM points.

Structure loss To preserve sharp geometric structures captured by the initial depth maps, MAtCha regularizes surface normals and mean curvature between the deformed charts and their initialization:

$$\mathcal{L}_{\text{struct}} = \sum_{i=0}^{n-1} \left(1 - N_i \cdot N_i^{(0)}\right) + \frac{1}{4} \sum_{i=0}^{n-1} \|M_i - M_i^{(0)}\|_1, \tag{A5}$$

where N_i and M_i are the surface normals and mean curvatures of chart i, while $N_i^{(0)}$ and $M_i^{(0)}$ are their counterparts derived from the initial depth maps.

Mutual alignment loss To enforce global coherence, MAtCha encourages neighboring charts to align by minimizing distances between projected overlapping points:

$$\mathcal{L}_{\text{align}} = \sum_{i,j=0}^{n-1} \sum_{u \in V_i} \min(\|\psi_i(u) - \psi_j \circ P_j \circ \psi_i(u)\|_1, \tau)\,, \tag{A6}$$

where V_i is the set of sampled UV coordinates on chart i, P_j is the projection from 3D space to the UV domain of chart j, and τ is the attraction threshold that limits the maximum alignment distance.

Final objective The overall optimization combines all three objectives:

$$\mathcal{L} = \mathcal{L}_{\text{fit}} + \lambda_{\text{struct}} \mathcal{L}_{\text{struct}} + \lambda_{\text{align}} \mathcal{L}_{\text{align}}, \tag{A7}$$

with $\lambda_{\text{struct}} = 4$ and $\lambda_{\text{align}} = 5$.

Although this alignment stage leverages cross-view projection constraints to yield more coherent scene geometry, its accuracy is ultimately limited by the quality of image correspondences. In regions with sparse or unreliable matches, it often introduces noticeable errors, motivating our plane-aware geometry modeling framework.

B.3 Gaussian Surfels Refinement in MAtCha

To further enhance the reconstruction of fine-grained scene structures through differentiable rendering, MAtCha introduces a Gaussian surfel refinement stage based on 2DGS. In this stage, surfels are iteratively optimized using a joint loss function that combines photometric consistency with geometric regularization terms.

RGB Loss The photometric loss is defined as a weighted combination of L1 loss and D-SSIM:

$$\mathcal{L}_{\text{rgb}} = (1 - \lambda)\mathcal{L}_1 + \lambda \mathcal{L}_{\text{D-SSIM}}, \tag{A8}$$

where $\lambda = 0.2$.

Regularization Loss The regularization loss consists of a distortion loss and a depth-normal consistency loss, as introduced in 2DGS.

To prevent surfel drifting and enforce cross-chart consistency, the distortion loss is applied:

$$\mathcal{L}_d = \sum_{i,j} \omega_i \omega_j |z_i - z_j|, \tag{A9}$$

where z_i denotes the intersection depth of the i-th surfel and ω_i is its blending weight.

To promote alignment of surface orientations across different charts, the depth-normal consistency loss is used:

$$\mathcal{L}_n = \sum_i \omega_i (1 - \mathbf{n}_i^{\mathrm{T}} \mathbf{N}_p), \tag{A10}$$

where $\mathbf{n}_i$ is the normal of the surfel and $\mathbf{N}_p$ is the normal derived from the depth gradient.

The overall regularization loss is then defined as:

$$\mathcal{L}_{\text{reg}} = \lambda_d \mathcal{L}_d + \lambda_n \mathcal{L}_n, \tag{A11}$$

with weight values $\lambda_d = 500$ and $\lambda_n = 0.25$.

Structure loss The structure loss follows a formulation similar to Eq. (A5):

$$\mathcal{L}_{\text{struct}} = \sum_{i=0}^{n-1} \|\bar{D}_i - D_i\|_1 + \sum_{i=0}^{n-1} \left(1 - \bar{N}_i \cdot N_i\right) + \frac{1}{4} \sum_{i=0}^{n-1} \|\bar{M}_i - M_i\|_1 \,, \tag{A12}$$

where $\bar{D}_i$, $\bar{N}_i$, and $\bar{M}_i$ are rendered from the Gaussian surfels, while D_i, N_i, and M_i are obtained from the charts.

Total refinement loss The complete optimization objective is given by:

$$\mathcal{L}_{\text{total}} = \mathcal{L}_{\text{rgb}} + \mathcal{L}_{\text{reg}} + \mathcal{L}_{\text{struct}}. \tag{A13}$$

During each round of 2DGS training, our method employs the same total loss formulation as MAtCha, but enhances it by computing D_i, N_i, and M_i in the structure loss term using our plane-aware geometry modeling. This integration of more robust geometric constraints leads to more accurate and consistent reconstructions.

C More Training Details

C.1 Merging Global 3D Planes

As described in Section 3.2, we merge 2D plane masks from different viewpoints by leveraging the 3D scene point cloud. To this end, we first compute the 3D point cloud corresponding to each 2D plane mask, and then evaluate the similarity between every pair of 3D point cloud sets using the overlap ratio. For computational efficiency, we project the entire 3D scene point cloud into all viewpoints at once. However, this projection process introduces two challenges: (1) along each camera ray, all points are projected onto the same pixel, which ignores occlusion; (2) when the surface points are insufficiently dense, some pixels may not receive projections from actual surface points but instead from points located behind the surface.

Both issues degrade the accuracy of global 3D plane merging. To address them, we first render the depth maps of all viewpoints using Gaussian surfels, and then back-project these depth maps to reconstruct the 3D scene point cloud. This ensures that every pixel in each viewpoint is associated with a valid surface point. Moreover, to account for occlusion, when projecting the reconstructed 3D scene point cloud into a given viewpoint, we compute the depth values of the points and require that their relative deviation from the Gaussian-rendered depth values does not exceed 1%.

These steps ensure that our global 3D plane merging process is both accurate and efficient.

C.2 Plane-aware Novel View Selection

As described in Section 3.3, we formulate the selection of plane-aware novel view camera centers as a search problem. The objective is to maximize the coverage of plane points, minimize the distance between the camera and the plane, and encourage the camera viewing direction to align with the corresponding plane normal.

Let the camera center be denoted by $\mathbf{c}$, the look-at point by $\mathbf{p}$ (*i.e.*, the center of the 3D plane), and the plane normal by $\mathbf{n}$. The optimization problem is then defined as:

$$\mathbf{c}^* = \arg\max_{\mathbf{c} \in \mathcal{C}} \Big(R(\mathbf{c}) + \big| \cos\theta(\mathbf{c}, \mathbf{p}, \mathbf{n}) \big| - D(\mathbf{c}, \mathbf{p}, \mathbf{n}) \Big), \tag{A14}$$

where $\mathcal{C}$ denotes the set of visible voxel centers in the visibility grid, $R(\mathbf{c})$ denotes the ratio of plane points visible from $\mathbf{c}$ to the total number of plane points. $\theta(\mathbf{c}, \mathbf{p}, \mathbf{n})$ is the angle between the viewing direction $(\mathbf{p} - \mathbf{c})$ and the plane normal $\mathbf{n}$, and $D(\mathbf{c}, \mathbf{p}, \mathbf{n})$ denotes the distance from the camera center to the plane.

In addition to our proposed plane-aware novel view selection strategy, we incorporate an elliptical trajectory around the scene center, following prior work (Wu et al., 2025c), to further enhance view diversity.

C.3 GEOMETRY-GUIDED INPAINTING

As shown in Fig. A3, training Gaussian representations with multi-view inconsistent inpainting results leads to black shadows in inconsistent regions, a phenomenon also observed in GuidedVD Zhong et al. (2025). To address this issue, GuidedVD constrains the diffusion denoising process to preserve observed regions, thereby alleviating inconsistencies near these regions. However, it remains ineffective for large missing areas (see Figs. 4 and A9) and suffers from slow training speed (see Table 3).

In contrast, our approach mitigates multi-view inconsistencies by incorporating scale-accurate geometry guidance throughout the generative pipeline (introduced in Section 3.3). Within this pipeline, we further introduce a strategy that modulates color supervision based on scale-accurate depth to reduce inconsistencies in inpainting results. Specifically, we first establish correspondences across views by depth projection before training the Gaussian representation. For each region, we primarily rely on color supervision from a single view: if the region lies on a 3D plane, we select the view that provides the most complete observation of that plane, ensuring consistent inpainting; for non-planar regions, we select the first view where the region is observed. These operations are executed in parallel via geometric projection, require only a single pre-processing step before Gaussian training, and thus incur minimal computational overhead.

As shown in Fig. A3, our approach substantially reduces the impact of multi-view inconsistencies, producing sharper and cleaner renderings.

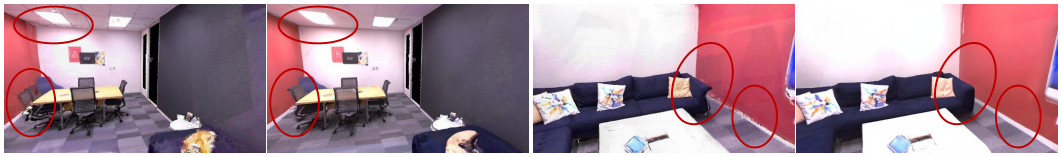

Incon. Results View1 | *Con.* Results View1 (Ours) | *Incon.* Results View2 | *Con.* Results View2 (Ours)

Figure A3: **Training results with inconsistent (*Incon.*) vs. consistent (*Con.*) multi-view inpainting.** Training Gaussian representations with inconsistent inpainting leads to black shadows in non-consistent regions, while our method significantly reduces such artifacts, yielding sharper and cleaner renderings.

C.4 CHOICE OF GENERATIVE MODELS

For the generative models in our experiments, we primarily use an inpainting-based diffusion model, *i.e.*, See3D (Ma et al., 2025). Note that our model is compatible with other models, such as the camera-controlled diffusion models like ZeroNVS (Sargent et al., 2024) or Stable Virtual Camera (Zhou et al., 2025). In such cases, the input images serve as references, while our selected novel views act as conditions. The visible masks can thus keep the visible areas unchanged while leveraging color supervision from viewpoints that observe the global 3D plane most completely. This capability is demonstrated in the single-view testing, as detailed in Appendix A.1.

C.5 DATASET DETAILS

For each scene, we uniformly sample 100 images. For ScanNet++ (Yeshwanth et al., 2023) and DeepBlending (Hedman et al., 2018), we randomly select 5 images as input views and use the remaining 95 images as test views. For Replica (Straub et al., 2019), we conduct three groups of experiments with 5, 10, and 15 input views to assess the performance under varying levels of view sparsity in Table A1. In all three Replica experiments, we use the same 85 test views to ensure a consistent evaluation set across settings.

C.6 EVALUATION METRICS

Rendering Metrics Following prior work (Guédon et al., 2025), we evaluate rendering quality using PSNR, SSIM and LPIPS computed with the VGG network (Simonyan & Zisserman, 2014).

Reconstruction Metrics Following prior work (Yu et al., 2022; Guédon et al., 2025), we evaluate the Chamfer Distance (CD) in cm, F-score with a threshold of $5cm$ and Normal Consistency (NC) for 3D scene reconstruction. These metrics are defined in Table A3.

C.7 Implementation Details

We implement our model in PyTorch (Paszke et al., 2019) and conduct all experiments on a single NVIDIA A100 GPU, except for the dense-view reconstruction results in Appendix A.2, which are obtained on a single NVIDIA 3090 GPU. As described in Section 3.4, after completing the initialization stage, we perform three geometry-guided generative training loops. In each loop, 10 additional views generated by See3D are incorporated into the training set. Both the initialization stage and each loop train the Gaussians for 7000 iterations.

As shown in Table 3, training a single scene from Replica *room_0* with 5 input views using our method takes slightly over one hour. In addition, we evaluate a variant with a downsampled number of Gaussians, which further accelerates training while maintaining competitive performance, as reported in the *Ours (DS)* entry of Table 3.

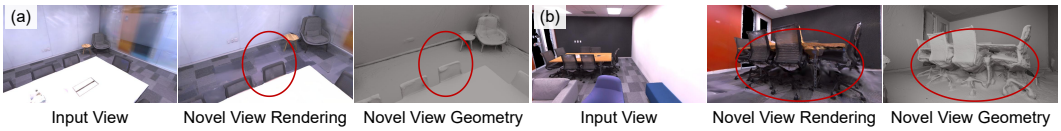

Figure A4: **Failure cases.**

D Failure Cases and Limitations

In this section, we present and analyze representative failure cases. As shown in Fig. A4(a), our method is partially limited by the capabilities of current video diffusion models. For example, video diffusion models such as See3D (Ma et al., 2025) often struggle to ensure that the colors in the completed regions exactly match those of the original scene. This can lead to inconsistencies when training Gaussians with the completed images, resulting in rendering outputs that do not fully align with the visible surrounding areas. Nevertheless, by introducing scale-accurate geometry supervision, our method can achieve precise geometry reconstruction even from inconsistent completions, as demonstrated in Fig. A4(a).

Fig. A4(b) illustrates another limitation: our approach struggles with heavily occluded regions, such as the chairs partially blocked by a table. Because the table and the occluded regions of the chair are in close proximity, generating a reasonable novel camera view of the occluded areas is challenging. We hypothesize that incorporating object-level prior (Ni et al., 2025; Yang et al., 2025) could help reconstruct such severely occluded regions.

Moreover, our method relies on the plane representation to obtain scale-accurate depth. While the monocular depth estimator used for non-plane regions yields satisfactory results in our experiments, we believe that adopting a more general surface representation, which can naturally model both plane and non-plane regions, could yield more accurate depth, particularly in non-plane areas. Although such a representation may be less computationally efficient than plane-based approaches, it is expected to improve overall reconstruction quality.

E LLM Usage Statement

The authors acknowledge the use of Large Language Models during the preparation of this manuscript. LLMs were employed solely to improve clarity of expression and to refine grammar throughout the text. All AI-generated suggestions were carefully examined, refined, and validated by the authors. The research contributions, experimental design, data analysis, and scientific conclusions remain entirely the original work of the authors.

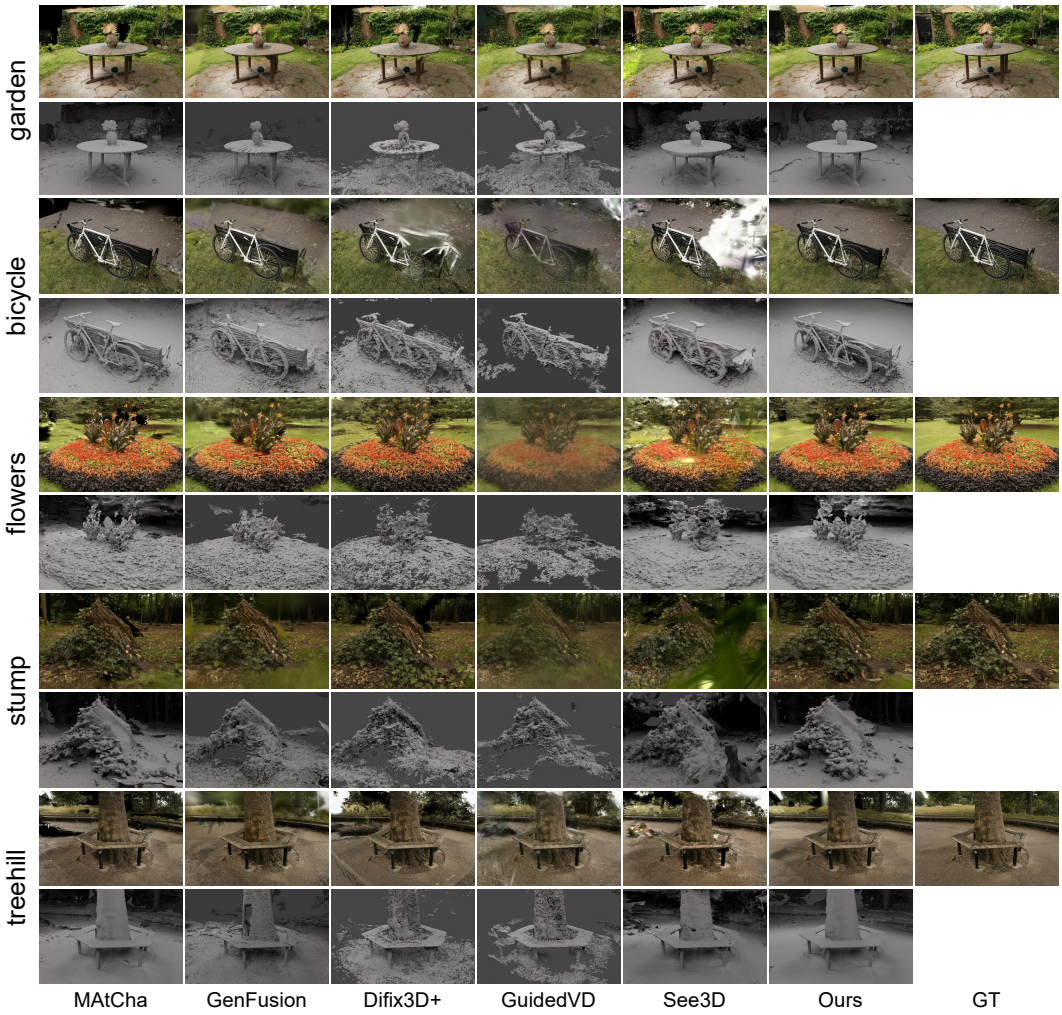

Figure A5: **Qualitative comparison using 9 input views on the Mip-NeRF 360 dataset.** We present results for all 5 outdoor scenes in the dataset. Our method produces significantly fewer Gaussian floaters and less blurriness, while recovering higher-quality and smoother geometry. These results demonstrate that our approach also performs robustly on non-planar and less structured outdoor scenes.

Table A2: **Quantitative results from 9 input views on the Mip-NeRF 360 dataset.** G4Splat performs strongly not only on indoor, Manhattan-style scenes (*bonsai, counter, kitchen, room*), but also on outdoor, non-Manhattan, and less structured scenes (*bicycle, flowers, garden, stump, treehill*), demonstrating its robustness in non-planar environments. Top-3 results are highlighted as the first, second and third.

	bicycle	bonsai	counter	flowers	garden	kitchen	room	stump	treehill	Mean
PSNR ↑										
MAtCha	15.56	15.36	15.96	13.66	17.94	18.96	17.16	18.52	14.80	16.44
GenFusion	16.50	17.93	17.96	14.37	18.43	19.76	19.80	19.82	15.79	17.82
Difix3D+	15.23	16.66	16.68	13.41	17.54	18.68	17.17	18.08	13.03	16.28
GuidedVD	14.89	17.21	17.60	14.23	18.23	18.00	18.50	19.00	13.36	16.78
See3D	16.08	16.32	16.49	15.80	19.94	19.62	18.23	18.26	11.51	16.92
Ours	18.31	17.97	19.94	15.48	19.18	20.84	20.71	19.53	15.99	18.66
SSIM ↑										
MAtCha	0.281	0.541	0.549	0.218	0.390	0.705	0.616	0.397	0.381	0.453
GenFusion	0.296	0.586	0.577	0.237	0.339	0.562	0.667	0.422	0.383	0.452
Difix3D+	0.227	0.551	0.497	0.185	0.288	0.530	0.568	0.339	0.313	0.389
GuidedVD	0.274	0.550	0.570	0.221	0.345	0.578	0.646	0.403	0.359	0.438
See3D	0.229	0.513	0.526	0.235	0.416	0.732	0.666	0.388	0.280	0.443
Ours	0.345	0.630	0.612	0.289	0.454	0.725	0.733	0.460	0.386	0.515
LPIPS ↓										
MAtCha	0.482	0.362	0.339	0.520	0.351	0.241	0.325	0.441	0.443	0.389
GenFusion	0.530	0.384	0.384	0.568	0.429	0.335	0.319	0.493	0.513	0.439
Difix3D+	0.509	0.370	0.378	0.529	0.408	0.311	0.350	0.474	0.501	0.426
GuidedVD	0.548	0.444	0.408	0.576	0.448	0.380	0.646	0.502	0.535	0.499
See3D	0.553	0.441	0.394	0.462	0.369	0.394	0.339	0.538	0.564	0.451
Ours	0.484	0.336	0.330	0.450	0.314	0.242	0.286	0.445	0.457	0.371

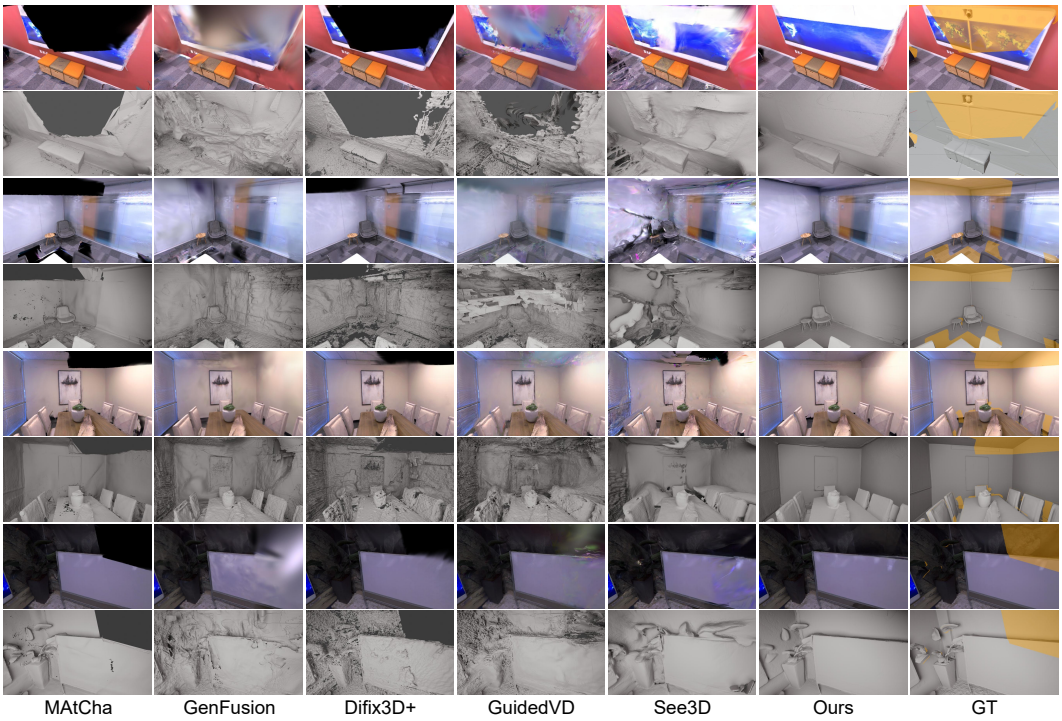

Figure A6: **Qualitative comparison from 5 input views with visibility mask.** In the GT images, golden regions indicate areas unobserved across the 5 input views. G4Splat not only improves reconstruction quality in regions visible to the input views compared to the baselines, but also achieves greater improvements in unobserved regions, producing smoother and more accurate geometry with fewer Gaussian floaters.

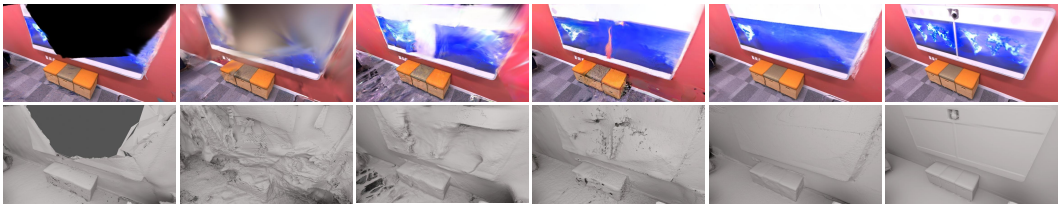

Figure A7: **Qualitative comparison from 5 input views.** Incorporating the See3D diffusion prior on top of MAtCha yields better results than applying it on 2DGS. The main reason is that MAtCha provides scale-accurate depth supervision. Although this depth is less accurate than the plane-aware depth in our method, it is still much more reliable than the depth distortion loss used in 2DGS.

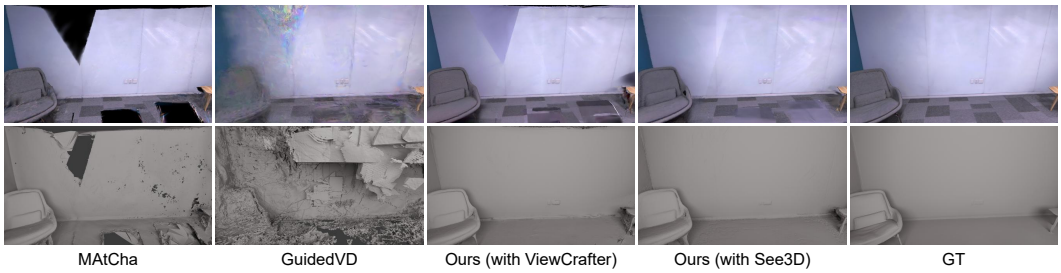

Figure A8: **Qualitative comparison from 5 input views using different diffusion models.** G4Splat produces high-quality, smooth geometry reconstruction even when paired with a weaker generative prior, and it continues to effectively suppress Gaussian floaters and reduce blurriness in the rendered results.

Table A3: **Evaluation metrics.** We show the evaluation metrics with their definitions that we use to measure reconstruction quality. P and P^* are the point clouds sampled from the predicted and the ground truth mesh. $\boldsymbol{n_p}$ is the normal vector at point $\boldsymbol{p}$.

Metric	Definition
Chamfer Distance (CD)	$\frac{Accuracy + \text{Completeness}}{2}$
Accuracy	$\underset{\boldsymbol{p} \in P}{\text{mean}} \left(\underset{\boldsymbol{p}^* \in P^*}{\min} ||\boldsymbol{p} - \boldsymbol{p}^*||_1 \right)$
Completeness	$\underset{\boldsymbol{p}^* \in P^*}{\text{mean}} \left(\underset{\boldsymbol{p} \in P}{\min} ||\boldsymbol{p} - \boldsymbol{p}^*||_1 \right)$
F-score	$\frac{2 \times \text{Precision} \times \text{Recall}}{\text{Precision} + \text{Recall}}$
Precision	$\underset{\boldsymbol{p} \in P}{\text{mean}} \left(\underset{\boldsymbol{p}^* \in P^*}{\min} ||\boldsymbol{p} - \boldsymbol{p}^*||_1 < 0.05 \right)$
Recall	$\underset{\boldsymbol{p}^* \in P^*}{\text{mean}} \left(\underset{\boldsymbol{p} \in P}{\min} ||\boldsymbol{p} - \boldsymbol{p}^*||_1 < 0.05 \right)$
Normal Consistency	$\frac{Normal\ Accuracy + Normal\ Completeness}{2}$
Normal Accuracy	$\underset{\boldsymbol{p} \in P}{\text{mean}} \left(\boldsymbol{n}_{\boldsymbol{p}}^T \boldsymbol{n}_{\boldsymbol{p}^*} \right)$ s.t. $\boldsymbol{p}^* = \underset{\boldsymbol{p}^* \in P^*}{arg\,min} ||\boldsymbol{p} - \boldsymbol{p}^*||_1$
Normal Completeness	$\underset{\boldsymbol{p}^* \in P^*}{\text{mean}} \left(\boldsymbol{n}_{\boldsymbol{p}}^T \boldsymbol{n}_{\boldsymbol{p}^*} \right)$ s.t. $\boldsymbol{p} = \underset{\boldsymbol{p} \in P}{arg\,min} ||\boldsymbol{p} - \boldsymbol{p}^*||_1$

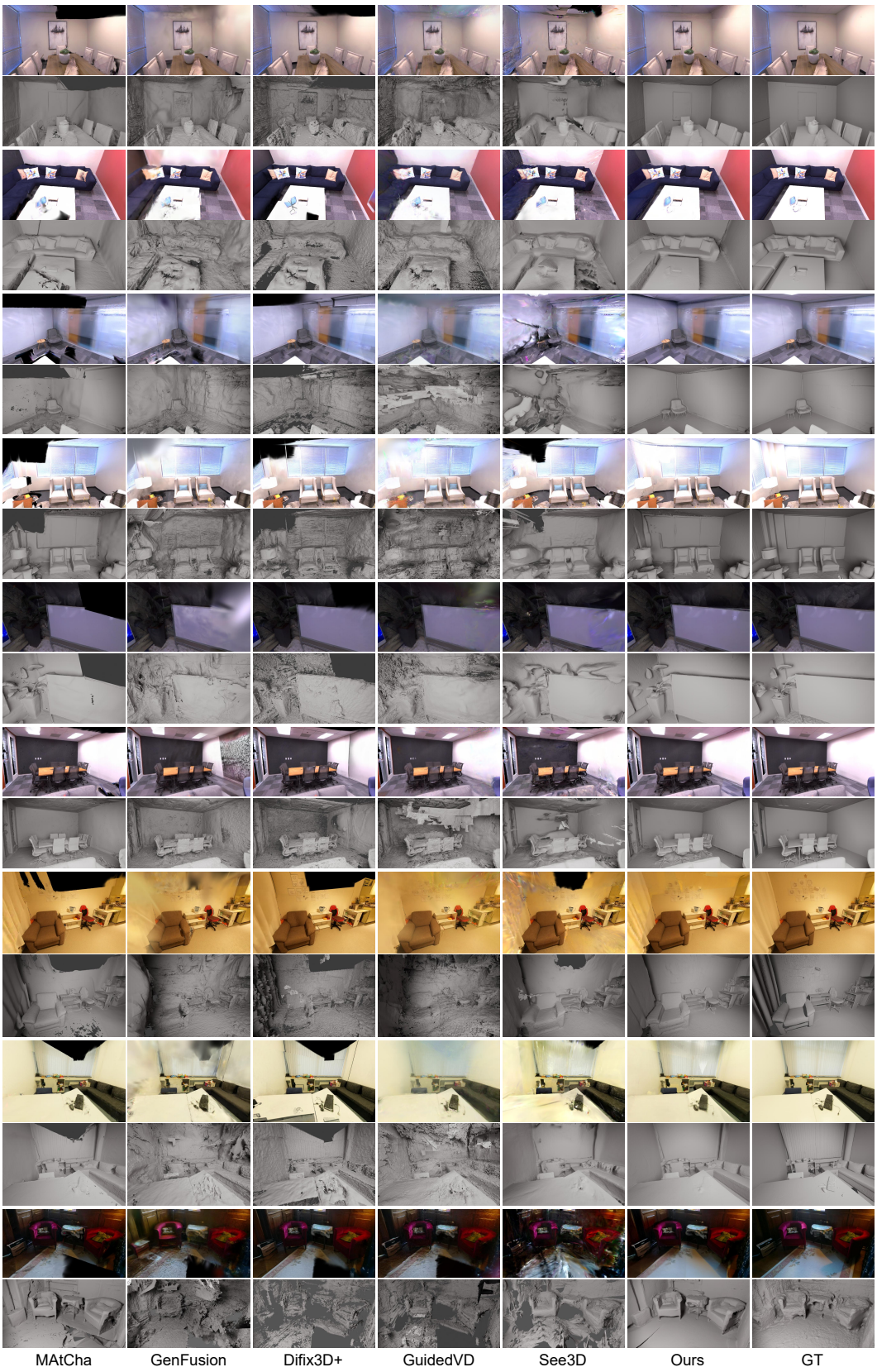

Figure A9: **More qualitative results.**